Statistical studies of chaotic wave patterns

B. J. Gluckman,* C. B. Arnold, and J. P. Gollub†
Physics Department, Haverford College, Haverford, Pennsylvania 19041
and Physics Department, University of Pennsylvania, Philadelphia Pennsylvania 19104
(Received 1 September 1994)

We present statistical measurements of spatially and temporally chaotic surface waves in relatively large containers (10–30 wavelengths across) with various boundary geometries and wetting conditions. The patterns are measured using transmission optics and video image processing. Although the instantaneous patterns are highly disordered, they retain sufficient phase coherence that the time-averaged images have spatially periodic structure. The symmetry of the time-averaged images is related to the symmetry of the boundaries. The convergence of the averaging process is significantly slower than that of a Gaussian random process. An average image can be explained as arising from amplitude and phase fluctuations about a base wave pattern. The *form* of the base pattern is that expected near onset in an infinite system. The amplitude of the average image, which decreases with drive amplitude, is related to the variance of phase fluctuations. Despite the relatively large dimensions, the base pattern is box quantized by the cell walls. Nonhysteretic jumps occur between these states as the drive frequency is varied. Close to the jumps the patterns fluctuate between several quantized states. Some of the statistical methods utilized here could be employed to analyze spatiotemporal chaos in other systems.

PACS number(s): 47.52.+j, 47.35.+i, 47.54.+r

I. INTRODUCTION

The problem of how to characterize and understand *spatiotemporal chaos* is a challenging issue in nonlinear physics. These states fluctuate not only in time but also in space and have correlation lengths sufficiently short that many degrees of freedom are involved in the dynamics. Many spatially extended systems exhibiting spatiotemporal chaos (STC) have been investigated, both experimentally and numerically, and a variety of methods have been employed to characterize them [1].

The invariant quantities used to characterize nonlinear dynamics (attractor dimension, Kolmogorov-Sinai entropy, and so forth) can be determined in *numerical* studies of STC, and methods have been proposed to determine some of them from experimental data [2]. However, the data requirements such that, so far, these methods have not been found generally useful. On the other hand, statistical methods have been productively employed to describe STC in some cases. For example, statistical properties of the total heat transport (e.g., averages, spectra, and moments) have provided a useful but limited way to characterize STC in thermal convection, starting with the early measurements of Ahlers and Behringer [3]. Analogous global measurements were employed in subsequent studies of other systems. The statistical properties of defects in STC have also been explored, especially in electroconvecting nematic liquid crystals [4,5]. The systematics of spatial autocorrelation functions have been used fruitfully to characterize STC in both parametrically forced surface waves [6] and Rayleigh-Bénard convection [7].

A variety of other statistical measures are accessible through imaging measurements. The simplest of these is the time average of the pattern, or of its image. Though this may seem like an obvious measure to consider, it has not been studied until recently in pattern forming systems, although it had earlier been considered in the study of dynamical systems [8–10].

One might expect on grounds of translational invariance that the spatial average of a sufficiently large thin layer system would be featureless in a state of spatiotemporal chaos, if the correlation length ξ is very much less than the horizontal dimension L. However, the approach to this limit, and the behavior of time-averaged patterns for large but not infinite systems, is less clear. In a preliminary paper [11], we explored the systematics of time averages in parametrically forced surface waves (Faraday waves) far above the onset of STC in square cells of widths up to 20 times the wavelength of the basic cellular instability. Structured time averages were found and noted to be aligned with respect to the walls of the container. (An example of this phenomenon is shown in Fig. 1; a full discussion of this figure and the relevant parameters appears later in the paper.) The amplitude of the average pattern decreased with increasing drive amplitude and the characteristic wave number was observed to change discontinuously as a function of drive frequency. The amplitude of the average pattern was also dependent on the degree of pinning of the meniscus at the lateral boundaries. The structured time averages apparently occur because the chaos involves small ordered patches that are preferentially aligned and partially phase coherent with

*Present address: White Oaks Lab, Naval Surface Warfare Center, Silver Spring, MD 20903.
†Corresponding author.
Electronic address: jgollub@haverford.edu

the average, despite the large chaotic fluctuations.

Structured averages are known to occur in other systems. For example, Taylor vortices apparently persist in a mean sense far above the transition to turbulence. However, they have not been studied quantitatively. Ning *et al.* [12] have also reported structured time averages in a study of chaotic roll structures in rotating Rayleigh-Bénard convection. They studied the phenomenon in both circular and polygonal cells, and showed that fluctuations in the total heat flux through the layer are correlated with fluctuations in the spatial structure.

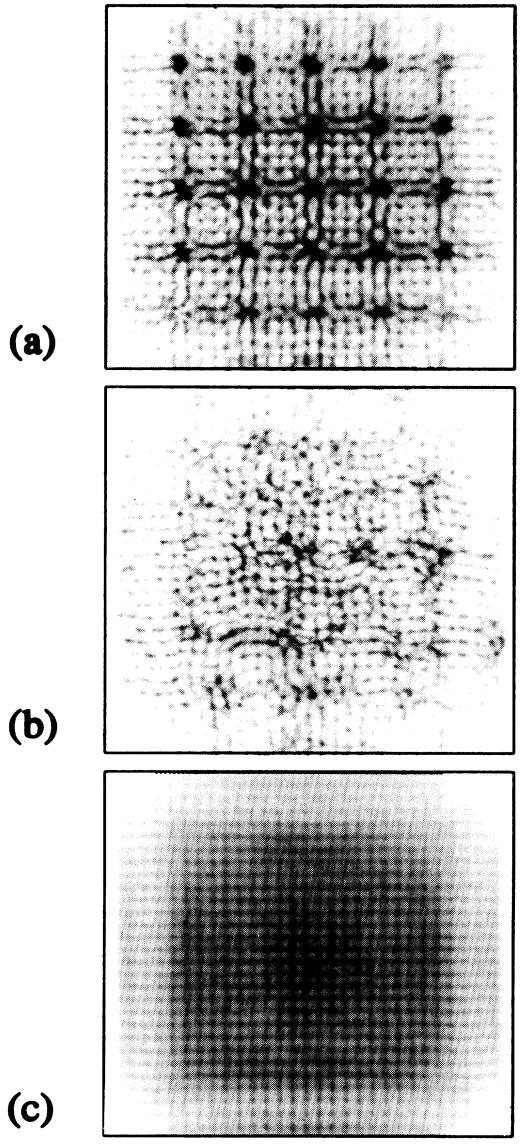

FIG. 1. Instantaneous and time-averaged images for square geometry (cell A, $f_0=55.75$ Hz). (a) Shadowgraph image of the time-independent wave pattern near onset ($\varepsilon=0.05$). The wave pattern is approximately a mixed mode with mode numbers (29,6). (b) Instantaneous image of a chaotic pattern ($\varepsilon=1.0$). (c) Time average over 12 800 images ($\varepsilon=1.0$). The average reveals the probability distribution of antinode positions. High intensities are shown dark.

In the present paper we extend our earlier studies of chaotic wave patterns, and show how the study of various statistical properties, including time averages, can be used to distinguish between competing hypotheses about the nature of the fluctuations. We characterize the average patterns precisely, and address the following questions: What determines the symmetry, amplitude, and wave number of time-averaged patterns? How do the averages compare with the patterns observed at onset, which are typically related to modes of the container? How can one best model the instantaneous patterns and their fluctuations in order to understand the emergence of the structured time averages? How do the patterns fluctuate about the mean pattern?

In order to place this work in context, and to explain the significance of these studies of the statistical properties of chaotic wave patterns, we begin by reviewing previous experimental and theoretical work on Faraday waves in Sec. II, with emphasis on studies related to spatiotemporal chaos. The experimental methods used in the paper are the subject of Sec. III. In Sec. IV, we introduce the structured time-averaged patterns, show their dependence on boundary symmetry, and demonstrate that their structure does not result from a trivial ordering of the whole pattern. In Sec. V we carefully explain how the time-averaged images can be interpreted to give information about the fluctuating instantaneous wave fields. We then present in Sec. VI extensive measurements and interpretation of the statistics and parameter dependence of the average images. A summary and discussion of the main results follows in Sec. VII.

II. RELATED WORK ON FARADAY WAVES

When a fluid layer with a free surface is subjected to a vertical oscillation of amplitude A greater than a critical value A_c, it is unstable with respect to interfacial standing waves. They were first studied and described by Faraday [13]; their nonlinear properties continue to provide interesting challenges. An extensive experimental and theoretical literature documents phenomena such as the development and selection of ordered patterns, and the subsequent transitions to spatial and temporal disorder.

The linear stability theory for waves on the surface of a fluid driven by vertical oscillation was developed by Benjamin and Ursell [14]. They considered the linear stability problem in the inviscid limit and solved for the velocity potential. Under the assumption that solutions are normal modes of the fluid container, the equations of motion reduce to the standard form for the Mathieu equation. The solution has stability tongues in the parameter space defined by drive acceleration vs wave number. The wave frequencies ω within the tongues occur at $\omega=n\Omega/2$, where Ω is the drive frequency and n is a positive integer. The $n=1$ subharmonic response is selected due to its lower threshold, after the effect of viscous dissipation is included in the theory. The dispersion relation connecting wave frequency ω and wave number κ is

$$\omega^2=\tanh(\kappa h)\left[\frac{\gamma}{\rho}\kappa^3+g\kappa\right], \tag{2.1}$$

where γ is the surface tension, ρ is the fluid density, g is the local gravitational constant, and h is the mean fluid depth.

Milner, and Zhang and Vinals [15] have extended the theory presented by Benjamin and Ursell to a set of amplitude equations that include nonlinear interactions between the spatial components of the waves. The resulting theory, applicable to large aspect ratio systems, predicts the wave number and symmetry of the most stable wave forms. For the fluid properties used in this paper, the theory predicts stable square patterns for a finite range above the critical amplitude:

$$\zeta(x,y)=a[\cos(\kappa x)+\cos(\kappa y)], \tag{2.2}$$

where the local surface height is denoted $h(x,y,t)=\zeta(x,y)\sin(\omega t)$, plus higher harmonics. For higher drive amplitudes, Milner predicted a secondary instability to a transverse amplitude modulation, similar to those observed in various experiments [6,16]. Additional phenomena due to a thin layer of surfactant at the interface, or a finite meniscus at the lateral boundary, have also been considered [15,17].

Experimental studies of onset patterns and transitions to disorder in Faraday waves were reviewed by Miles and Henderson [17]. Most experiments involve systems at low aspect ratio Γ, defined by the ratio of the cell size L to the hydrodynamic wavelength λ. Onset patterns were studied extensively by Douady and co-workers [18,19] in square and rectangular cells, with aspect ratios in the range $1<\Gamma<10$. They observed strong effects on pattern selection due to finite cell size and boundary wetting; the onset patterns were found to be modes of the container and linear combinations of these modes.

Disordered patterns at large aspect ratio were reported by Ezerskii *et al.* [16]. They observed the onset of transverse amplitude modulations not far above the wave onset, and proposed a phenomenological amplitude equation model to describe the resulting dynamics. Ezersky and Matusov [20] found that the addition of random noise reduced the threshold of the transition to STC. Recent work by the same group [21] concentrates on the dynamics of domain walls in large aspect ratio systems.

A statistical analysis of the transition to spatiotemporal chaos in Faraday waves at moderately high aspect ratio (50–100) was conducted by Tufillaro and coworkers [6,22], with *n*-butyl alcohol as their working fluid. The ordered patterns were locally square symmetric. They investigated the systematics of spatial correlation functions as the reduced drive amplitude $\varepsilon\equiv(A-A_c)/A_c$ was varied. They found that the transition to STC was marked by a sharp decline in both the correlation length ξ and the long-range orientational order of the pattern. In addition, they observed approximately Gaussian fluctuations in the underlying spatial Fourier amplitudes in the chaotic regime. The transition to STC was found to be dependent on cell geometry despite the fairly large aspect ratio. Edwards and Fauve [23] have recently suggested an explanation for this dependence based on the relatively narrow width of the stability tongues for low viscosity fluids.

Another approach to detecting the transition to spatiotemporal chaos was taken by Ciliberto, Douady, and Fauve [24]. They measured fluctuations in the total energy dissipated by the surface wave motion, via small fluctuations in the acceleration of the cell, which is driven at constant power. They found that these fluctuations are related to observed pattern fluctuations; therefore statistics of the energy dissipation could be used to identify the state of the waves.

Afraimovich *et al.* [25] have proposed a method for calculating the correlation dimension D_c of STC data in physical space rather than in phase space, and have applied it to the analysis of chaotic wave data. They find that as ε is increased over the range 0.15 to 1.85, D_c, calculated from individual instantaneous images of the waves, increases; the method appears to converge sufficiently: the variations between different measurements at the same ε are small.

In a recent investigation of spatiotemporal intermittency in Faraday waves at aspect ratio ~ 45, Bosch and van de Water [26] used measurements of the mutual information and spectral techniques in order to characterize the disorder in the waves. They observed non-Gaussian fluctuations of the spectral power at wave numbers smaller than the primary wave number of the pattern. These authors interpreted their observations in terms of coherent structures and the existence of long-range order.

In a subsequent study, Bosch, Lambermonti, and van de Water [27] confirmed the existence of time average patterns for chaotic surface waves in square cells for $\Gamma\sim 17$ and $\varepsilon<0.6$. They prefiltered their images in order to extract the positions of the antinodes, and observed ordered patterns in the distribution of antinode positions. They also noted a strong dependence on wetting conditions at the cell boundaries: the case for which the meniscus was "pinned" showed a lower rms node "velocity" and more pronounced hysteresis through the order-disorder transition than was the case when the meniscus was free. In addition, they observed longer correlation lengths along an axis aligned with the container walls than along the diagonals.

The disordered waves have also been explored by studies of particle and dye transport [28,29]. The statistics of single particle diffusion approach that of a Brownian process as the degree of disorder is increased. On the other hand, recent studies of relative particle diffusion by Alstrøm *et al.* [30] imply long-range correlations even for strongly disordered waves (large ε).

In summary, much of the previous work on Faraday waves has been concerned with describing the formation of patterns near the onset of the instability, and their subsequent *transitions* to disorder. Limited work has been done on the disordered states themselves. Understanding the disordered regime is the primary problem addressed in this paper.

III. EXPERIMENTAL METHODS

A. Apparatus

The automated experimental system is shown in Fig. 2(a). The fluid cell is mechanically coupled to a precision electromechanical vibrator (Vibration Test Systems VG100) controlled by a frequency synthesizer (Hewlett Packard 3325) and power amplifier. A piezoelectric accelerometer is used to monitor the acceleration amplitude. The maximum fluctuations in drive acceleration, observed at the high drive amplitudes due to variations in energy dissipation in the fluid, are approximately 2% rms. Provisions are made for optical access, and the whole system is enclosed in a large thermally controlled box and maintained at constant temperature $T=29\pm1\,^{\circ}\mathrm{C}$.

The fluid cell is a sealed box, with interior dimensions 2 cm deep by 10.5 cm square horizontally, and with a glass cover and bottom. The walls of the cell are machined from Delrin. Inserts are used to convert to alternate interior geometries, including square, circular, and slightly elliptical cavities. The elliptical cavity was made by matching a circular insert from a Delrin block while it was under compression in one direction, then allowing it to relax. The eccentricity of the resulting cell is $2(r_1-r_2)/(r_1+r_2)=0.02$, where r_1 and r_2 are the major and minor radii. The fluid is n-butyl alcohol (kinematic viscosity $\nu=2.8\ \mathrm{cm^2\,s^{-1}}$, surface tension $\gamma=24.6$ dyne $\mathrm{cm^{-1}}$, density $\rho=0.81\ \mathrm{g\,cm^{-3}}$). It wets the walls of the container. The cell is typically filled to a depth of 8 mm; the drive frequency is in the range $25<f_0<200$ Hz. A summary of the different cavity geometries is given in Table I.

In order to study the role of boundaries, several different types of boundary conditions are used in these experiments, as illustrated in Fig. 2(b). For the majority of the measurements, the free surface of the fluid is bounded by vertical walls, a case we call "wetted" boundaries. Additional measurements are made using "brim-full" boundaries, where the cell is filled to meet the corner of a horizontal step in the vertical walls. We also use an "over-full" case, in which the fluid layer is slightly higher than brim full, so that a thin layer (<1 mm) of fluid extends beyond the step.

B. Optics

The optics are based on screenless shadowgraph optics [31], as illustrated in Fig. 2(a). A collimated beam of white light, formed from a point source and a large diameter collimating lens, is sent vertically through the fluid surface. The light is collected and imaged onto the charged-coupled device (CCD) array of a video camera by a large collection lens and a camera lens. These lenses are kept at constant separation, approximately confocal. Different object planes are then selected by adjusting the distance from the camera lens to the CCD. The video signal from the camera is digitized by an Imaging Technologies image processor in a Sun workstation.

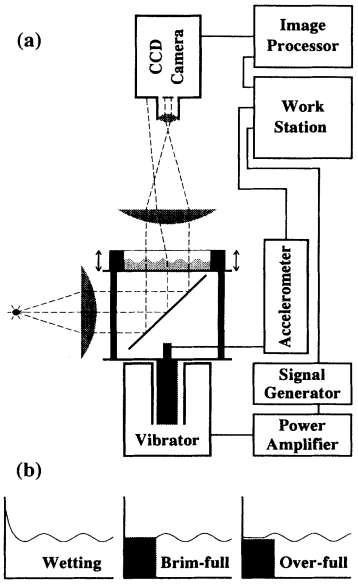

FIG. 2. (a) Experimental setup and optics. (b) Illustration of various boundary conditions utilized to explore the effects of wetting.

The acquired images are fairly insensitive to the sampling time provided that it is greater than one-half wave cycle and shorter than the dynamic time scale of the observed pattern fluctuations. To obtain what we call an "instantaneous" image, the light is integrated over a full video frame (1/30 s), a time sufficiently long to integrate over more than one wave cycle. (For low driving frequencies some additional integration is performed after digitization in order to satisfy this requirement.) For each data run, the illumination intensity and the video digitization offset and gain are set to maximize the contrast and minimize the background in the instantaneous im-

TABLE I. Fluid cells.

Cell	Cavity geometry	Dimensions (cm)	Boundary conditions
A	Square	$L=10.5$	wetted
B	Square	$L=6.5$	wetted, brim full, over full
C	Circular	$R=3.5$	wetted
D	Elliptical	$R_{\mathrm{major}}=3.51$ $R_{\mathrm{minor}}=3.46$	wetted
E	Triangular, right isosceles	$L_1=L_2=10.5$ $L_3=14.8$	wetted

ages. Individual images or series of consecutive images can be stored for later analysis, or summed in real time to determine long time averages. We denote the "instantaneous" image by $I(\vec{x},t)$, and the (long) time average of the measured images by $A(\vec{x})\equiv\overline{I(\vec{x},t)}$. Typical averaging times are about 15 min; this corresponds to approximately 13 000 instantaneous images.

1. Shadowgraph technique

Although shadowgraph imaging is widely used for visualization of fluid systems, it is typically applied to systems where small gradients in the bulk properties result in local gradients in the index of refraction transverse to the light path. In that case, the deflection of the light rays is slight, and intensity variations in the resulting images are approximately linear in the square of the gradient of the index of refraction [31]. In contrast, we use the technique to visualize the deformation of the fluid surface. In this case, the deflection of the light due to refraction can be quite large, and much of the light is lost due to the finite apertures of the optics. The resulting images are therefore bright *only* where the local surface slope is close to zero. The images are similar to those produced by the reflection optics discussed by Douady [19].

The apertures of the optics limit the angle ϕ by which a ray can be deflected at the interface and still be detected, such that $|\tan\phi|\approx\phi<0.012$ [32]. This condition translates into a maximum surface gradient $\vec{\beta}\equiv\vec{\nabla}\zeta$ such that

$$|\beta|<0.026\equiv\Lambda \tag{3.1}$$

in order for light to pass through the optics to the CCD. We choose the mean surface of the fluid to be the object plane of our imaging system. A light ray refracted from a point at the fluid surface appears to originate at a point spatially offset from its actual position by $\zeta\sin\phi<0.012\zeta$. This offset is typically smaller than the spatial resolution of the measurement, and can be neglected. Therefore rays which pass through areas of the surface with $|\beta|<\Lambda$ are detected *without spatial offset* while all other rays are lost. This situation is illustrated in Fig. 2(a), where the rays drawn through the antinodes of the fluid surface propagate through to the CCD, while others do not pass through the camera lens aperture.

2. Computation of the images

The instantaneous optical images are not linear in the surface wave field, but they do have a simple interpretation, which is the subject of this section. The main point can be understood by considering an idealized case of one-dimensional standing waves of the form $\zeta(x)=a\cos(\kappa x)$, for which the gradient $\beta(x)=-a\kappa\sin(\kappa x)$. From linear theory for Faraday waves [15] we know that $a\kappa\sim\sqrt{\varepsilon}$. The proportionality constant is of order unity. It follows that for $\varepsilon>10^{-3}$ large areas of the images will appear dark. The majority of the present work is performed in the range of ε between 0.1 and 3.0. Therefore, *the images are sharply peaked functions which highlight the local extrema of the surface.* Because bright spots appear for both the maxima and minima, the images have *twice* the basic wave number of the surface height pattern.

In order to confirm this result, we compare two different calculations of the detected image for the same ideal wave form: one made by numerically tracing individual rays through the surface and the individual optical elements, the other computed by using a function approximately equal to a δ function of the local surface gradient. The results are shown in Fig. 3. We have utilized an

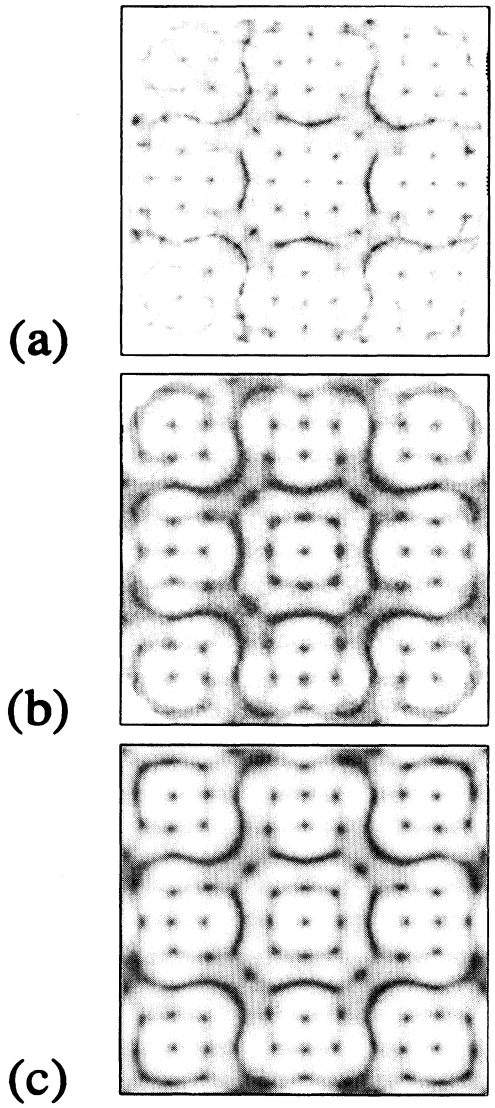

FIG. 3. Quantitative test of the imaging process. (a) Sample image of an onset pattern in the square cell. (b) Ray-tracing computation of the image, averaged over a cycle of the wave pattern. (c) Analytic approximation to the optical intensity $I_\delta(\vec{x})$ (Eq. 3.4). The waveform used is a positive mixed mode [Eq. (3.2)], with mode numbers (11,3). Bright spots in the image (shown dark here) appear at positions of small surface slope, i.e., at antinodes. The apparent wave number of the pattern is doubled.

idealized mixed mode wave form that is typical of patterns *near onset* in a square cell:

$$\zeta(x,y)=a(S_{mn}(x,y)\pm S_{nm}(x,y)) , \tag{3.2a}$$

where

$$S_{mn}(x,y)=\sin(m\pi x/L)\sin(n\pi y/L) . \tag{3.2b}$$

This function is a mixed mode that obeys Neumann boundary conditions for a square cell of length L, with the origin chosen at one of the corners of the cell. The mode numbers ($m=11$, $n=3$) are chosen to approximate the onset pattern shown in Fig. 3(a). For the computations we have chosen the wave amplitude such that $(ak)^2\sim\varepsilon=0.15$.

The ray tracing computation of the light intensity on the CCD is shown in Fig. 3(b). It is performed by tracing a large number of individual rays through the fluid surface and the subsequent optics. For each ray, a random temporal phase is chosen for the wave in order to accomplish the desired temporal integration. All of the rays are initially oriented vertically but pass through randomly selected locations. If a ray passes through the optics and reaches the CCD, the corresponding bin of a two-dimensional array is incremented. This process is repeated for approximately 10^7 rays to accumulate good statistics.

We used the actual material parameters and dimensions of the cell and the optics in this computation. However, we did not include either nonuniformity and imperfect collimation of the illuminating light, or lens aberration. The computed images are in good agreement with the observed onset patterns. This can be seen by comparing Fig. 3(a) with 3(b). We have also performed this calculation without temporal integration. The same sharp structure occurs for the peaks, but the constant intensity background between the peaks is not present in that case.

We also find that the following model is a useful approximation for the instantaneous images:

$$I(\vec{x},t)\cong I_0\delta(|\vec{\nabla}\zeta(\vec{x},t)|)$$

$$=I_0\delta(\partial_x\zeta(\vec{x},t))\delta(\partial_y\zeta(\vec{x},t)) . \tag{3.3}$$

That is, that the instantaneous image is proportional to a δ function of the local slope of the surface height. This model is obtained from two related facts: (a) for light to be detected, the surface-height gradient must be less than a small value Λ, and (b) the light that is detected is not significantly deflected from its original path. In the limit that $\Lambda\to 0$ these conditions yield (3.3). In order to generate images directly from an ideal wave form, and to include the fact that Λ actually has a finite value, we use the following analytic approximation that has the correct limiting behavior:

$$I_\delta(\vec{x},t)=I_0\Lambda^2/(\Lambda^2+\beta^2(\vec{x},t)) , \tag{3.4}$$

where $\beta^2\equiv\vec{\beta}\cdot\vec{\beta}$. This function, applied to the same ideal wave form as in Fig. 3(b), is shown in Fig. 3(c). The result is in good agreement with the ray-traced image of Fig. 3(b), although it does not reproduce the radial effects observed at the corners of the ray-traced image and actual images, nor the diffuse background associated with the temporal integration. [The radial effects are primarily due to the aperture of the first lens, and are neglected in the derivation of (3.1).] The result is not strongly dependent on the value chosen for Λ. We conclude that the model of (3.4), or even the δ function limiting behavior of (3.3), is well founded.

IV. EXPERIMENTS: BASIC OBSERVATIONS

In this section we introduce the phenomenon of structured time-averaged images and present examples observed in cavities of different shapes. In Sec. IV A we show the relationship between the symmetry of the average pattern and that of the container. In Sec. IV B, we use time-dependent statistics of the instantaneous patterns to show that the structure in the average images does *not* result from occasional ordering of the *entire* instantaneous pattern; instead the structure results from small patches of the instantaneous pattern that are ordered and in phase with the average pattern. Finally, in Sec. IV C, we discuss the time-dependent convergence of the averaging process.

A. Boundary symmetry

Our interest in time averages was originally motivated by the ideas presented in Refs. [8–10], the authors of which investigated dynamical systems represented by mappings and differential equations defined on symmetric spatial domains. They discussed dynamical transitions that change the symmetry of the invariant measure of the attractors in phase space, and argued that these symmetry-changing bifurcations would be manifest in physical space through the time averages of appropriate physical variables. Our measurements of chaotic Faraday waves provide a possible system in which to explore these ideas. Therefore, we chose cells with several different types of symmetry. The characteristics of the various cells are summarized in Table I.

1. Square cell

Typical images taken in a square cell are shown in Fig. 1. The stationary pattern [Fig. 1(a)], observed just above the onset of the Faraday instability, is a standing wave that conforms both to the dispersion relation and the boundary conditions; it is similar to the mixed modes described by (3.2). (For a complete discussion of onset patterns, the reader is referred to Douady and Fauve [18].) For sufficiently high drive amplitudes, i.e., $\varepsilon>0.1$ for these cavity and fluid parameters, the stationary patterns are unstable and the waves become disordered in both space and time.

A disordered instantaneous image in the chaotic regime is shown in Fig. 1(b). In addition, a series of images from the central region of the cell, spaced 4.5 s apart, is shown in Fig. 4. The instantaneous images display small patches of locally ordered square symmetric waves, as seen for example in the center of the lower left image of Fig. 4. The patches are interspersed with many defects,

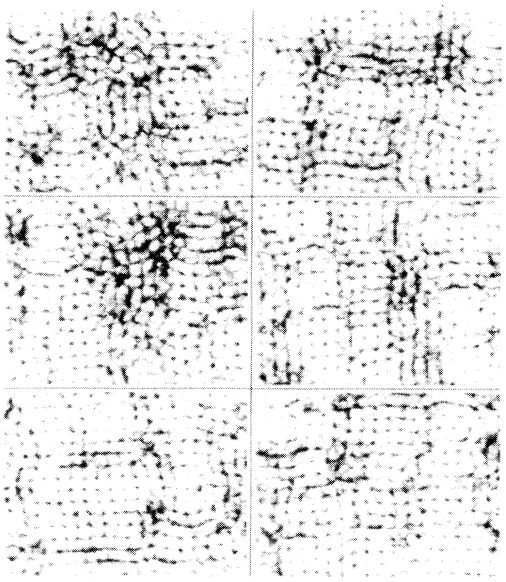

FIG. 4. Series of six instantaneous images of chaotic waves in square cell A at 4.5 s intervals ($f_0=55.75$ Hz, $\varepsilon=1.0$). The central region of the cell is shown; time increases downward, then across.

and the number of defects fluctuates in time. The orientations of the patches also vary, although a visual inspection suggests that they are affected by the boundaries.

To estimate the degree of disorder in the instantaneous pattern, we determine the correlation length from the spatial autocorrelation function

$$G(\Delta\vec{x})=\langle \Delta I(\vec{x},t)\Delta I(\vec{x}+\Delta\vec{x},t)\rangle_{\vec{x}}/\langle \Delta I^2\rangle_{\vec{x}}\ , \qquad (4.1)$$

where $\Delta I(\vec{x},t)\equiv I(\vec{x},t)-A(\vec{x})$ [33]. The computations include the central region $L/6<(x,y)<5L/6$ and are ensemble averaged over a series of instantaneous images. This function is shown in Fig. 5(a). A one-dimensional cut through $G(\Delta\vec{x})$, shown in Fig. 5(b), reveals a sharp central peak, a decaying oscillatory tail, and possibly a slowly varying baseline. The sharp central peak is due to imaging nonlinearity, and we do not attempt to describe the correlation function for small Δx. We attribute the slight baseline variation to nonuniformity of the illumination. The peak-to-peak amplitude $|\Delta G|$ of the oscillatory tail can be approximated by a decaying exponential, as shown in the inset of Fig. 5(b). We use the decay length as a measure of the correlation length. We note that the data could also be described approximately by a power law. However, the correlation length obtained in the manner described here is in reasonable agreement with estimates obtained in other ways, e.g., the inverse bandwidth in Fourier space. We find that the correlation length for the conditions of Figs. 1 and 4 is 2.0 ± 0.2 cm. This value is approximately six times the dominant image wavelength, or 20% of the container width. It decreases slowly with ε.

The time-averaged image $A(\vec{x})$ is shown in Fig. 1(c). It is square symmetric and aligned with the boundaries. The average image is significantly different from the image observed near onset; it lacks the long-wavelength modulation of the onset pattern. In the central region, the wavelength and oscillation amplitude are nearly constant. These properties are shown graphically in Fig. 6, where we plot $A_y(x)\equiv\langle A(\vec{x})\rangle_y$ over the range $L/4<y<3L/4$ as a solid line. (For reference, we also plot the corresponding spatial average for the stationary image observed at onset, offset vertically.) The intensity

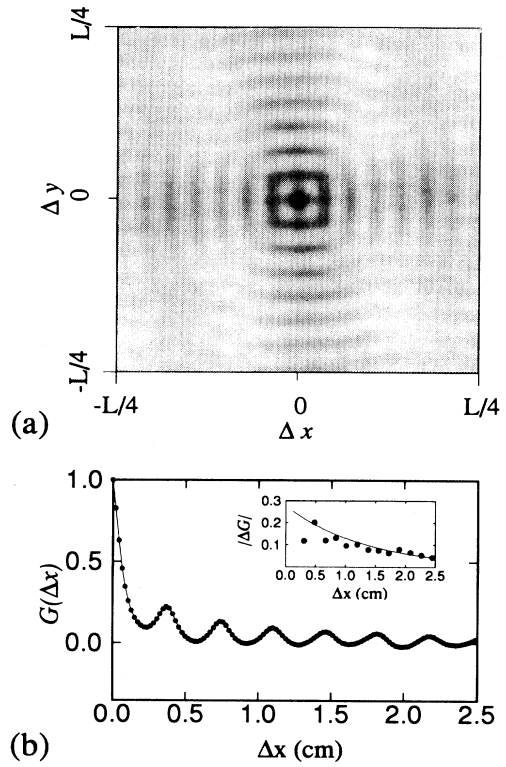

FIG. 5. Autocorrelation function, $G(\Delta\vec{x})$ of instantaneous images of chaotic waves (square cell A, $f_0=55.75$ Hz, $\varepsilon=1.0$). (a) Two-dimensional inverted gray scale image. (b) One-dimensional cut at $\Delta y=0$. The inset shows the peak-to-peak amplitude, and a fit to a decaying exponential. The correlation length is approximately 20% of the width of the cell.

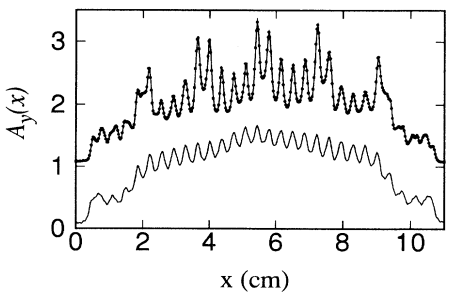

FIG. 6. Averages over y of the time-averaged images (solid line) and the time-independent onset state (line with dots, offset vertically), from Fig. 1. The time average is oscillatory but lacks the slower modulation shown by the onset image.

of the average image goes to zero at the boundaries of the cell mainly because the meniscus imposes nonzero slope at the walls; there is also a slow spatial variation due to the illumination, which is maximal at the center of the cell.

In order to test whether the average images are repeatable (as opposed to varying on even longer time scales), we have performed consecutive time averages for 15 min using the same drive parameters. The resulting averages are essentially identical: the rms difference is less than 2% of the mean, and their wave numbers and phases are identical. Average images obtained after reducing the drive acceleration to zero between measurements are also essentially identical.

2. Circular cell

Images for a circular cavity are shown in Fig. 7. The onset pattern [Fig. 7(a)] is a standing wave pattern with eightfold rotational symmetry, of the form $\zeta = a_0 J_0(\kappa_0 r) + a_8 J_8(\kappa_8 r)\sin 8(\theta - \theta_0)$ plus higher harmonics. This pattern is significantly different from the square wave patterns that would be observed for these fluid parameters in an infinite cell. A typical instantaneous image obtained in the chaotic regime at higher driving amplitude ($\varepsilon = 0.5$) is shown in Fig. 7(b). As is the case for the square container, the instantaneous patterns show evidence of local fourfold symmetry in small patches, and orientational changes from patch to patch. Finally, the average image for the circular cell is shown in Fig. 7(c). In contrast to both the onset image and the instantaneous images, the average image has full rotational symmetry.

3. Other geometries

The results from chaotic patterns in a slightly elliptical cavity, cell *D*, are shown in Fig. 8 for $f_0 = 100$ Hz. At relatively low drive amplitude, $\varepsilon = 0.15$, the instantaneous images are time dependent and reasonably disordered in space, with local patches of approximate fourfold symmetry. An example is shown in Fig. 8(a). The time average image is highly asymmetric [Fig. 8(b)]. It has the same set of reflection symmetries as the cavity. The contrast at the center of the pattern is strong, but there are large areas of low contrast along the major axis which are absent along the minor axis. At higher drive amplitude the average image is nearly circular, as shown for $\varepsilon = 0.50$ in Fig. 8(d). The regions of low contrast have disappeared, and the eccentricity of the average is now approximately that of the cavity. Summarizing, we find that the *asymmetry* of the average image in a slightly distorted geometry decreases with increasing disorder in the waves.

Some exploratory work was also performed in an isos-

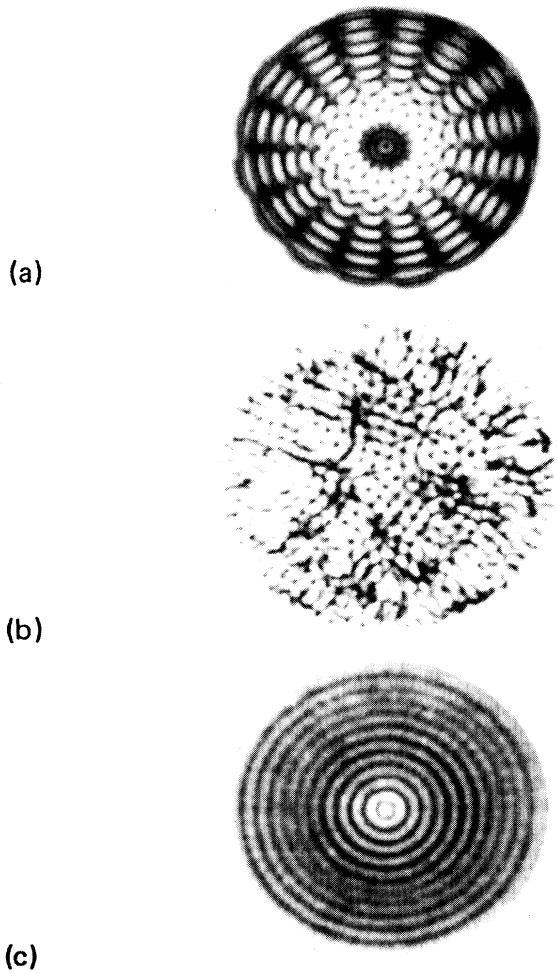

FIG. 7. Instantaneous and time average images for circular geometry (cell *C*, $f_0 = 81$ Hz). (a) Shadowgraph image of time-independent wave pattern near onset ($\varepsilon = 0.01$). (b) Instantaneous image of a chaotic pattern ($\varepsilon = 0.5$). (c) Time average over 12 800 images or ~ 15 min ($\varepsilon = 0.5$).

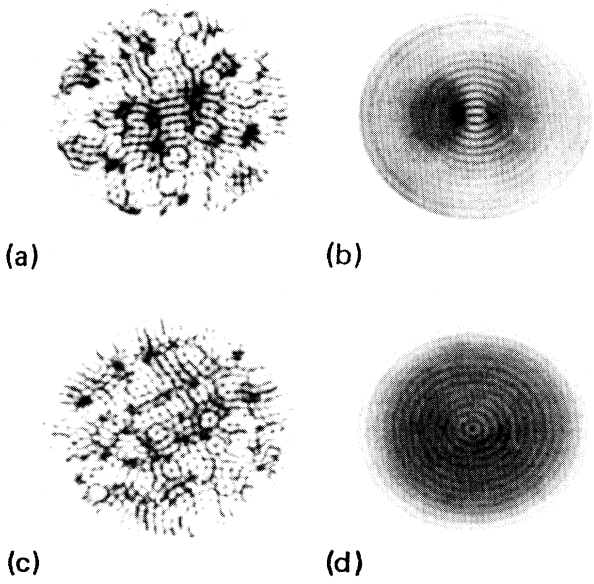

FIG. 8. Instantaneous [(a) and (c)] and time-averaged [(b) and (d)] images in a cell with ellipticity 0.02 at $f_0 = 100$ Hz. [(a) and (b)] $\varepsilon = 0.15$; [(c) and (d)] $\varepsilon = 0.50$. The asymmetry of the resultant image is amplified at the lower drive amplitude, and is less pronounced at higher ε.

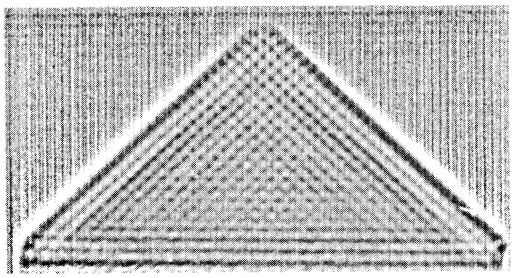

FIG. 9. Enhanced time-averaged image observed in the triangular cell E ($\varepsilon=1.5$).

celes triangular cell, created by bisecting square cell A along a diagonal. Structured time averages were again found, as shown in Fig. 9, but seemed too complex for extended study.

4. Summary

Qualitatively we observe that images of spatially and temporally chaotic wave patterns can have highly ordered, structured time averages in various geometries. Although the instantaneous images show local fourfold rotational symmetry, as predicted by theory for these fluid parameters, the symmetry of the average images is determined by the boundaries.

B. Time-dependent cross correlation coefficient

We now address the question of how the average images develop from a sequence of instantaneous images. The following are two possible scenarios: (i) The instantaneous patterns fluctuate randomly, but occasionally pass through fully ordered states which are closely aligned with the average; and (ii) the instantaneous patterns fluctuate chaotically, are never fully ordered, but are somehow biased toward the average. In order to probe the proximity of the instantaneous image to the average image, we calculate the cross correlation coefficient between the spatial fluctuations of the average and instantaneous images as a function of time, $G_{IA}(t)$:

$$G_{IA}(t)\equiv\langle\delta A(\vec{x})\delta I(\vec{x},t)\rangle/\delta A_{\rm rms}\delta I_{\rm rms}\ , \tag{4.2}$$

where the angular brackets denote averages over space, and where $\delta A\equiv A-\langle A\rangle$ and $\delta I\equiv I-\langle I\rangle$ denote the subtraction of the spatial mean. This function approaches unity for instantaneous images that are optimally correlated or aligned with the average, and approaches zero for images that are completely uncorrelated. It has a positive mean value, provided that the average image has non-zero structure. This can be seen as follows:

$$\overline{G_{IA}(t)}=\frac{\overline{\langle\delta A(\vec{x})\delta I(\vec{x},t)\rangle}}{\delta A_{\rm rms}\delta I_{\rm rms}}=\frac{\langle\delta A(\vec{x})\overline{\delta I(\vec{x},t)}\rangle}{\delta A_{\rm rms}\delta I_{\rm rms}}$$
$$=\frac{\langle\delta A(\vec{x})\delta A(\vec{x})\rangle}{\delta A_{\rm rms}\delta I_{\rm rms}}=\frac{\delta A_{\rm rms}}{\delta I_{\rm rms}}\ . \tag{4.3}$$

We have assumed that the normalization, $\delta A_{\rm rms}\delta I_{\rm rms}$, is constant in time. This assumption is valid to within $\sim 1\%$.

1. Square symmetry

The time-dependent cross correlation coefficient is shown in Fig. 10(a) for a series of 500 images at $\varepsilon=1.5$. The images are spaced 0.3 s apart. We consider only the central fourth of the cell in order to avoid wall effects. The signal-to-noise ratio in Fig. 10(a) is roughly six, so some of the small fluctuations are not significant. We find a mean correlation of approximately 0.16, with a standard deviation of about 0.10. The characteristic correlation time is about 2.2 s. The fluctuations in Fig. 10(a) are not far from Gaussian, and no events with correlations above 0.5 are found. These observations exclude scenario (i), in which the instantaneous pattern would show occasional spikes of very strong correlation with the average, but are consistent with scenario (ii).

It is useful to inspect the time- and space-dependent function $\delta A(\vec{x})\delta I(\vec{x},t)$, the space average of which yields $G_{IA}(t)$. Sequences of snapshots of this function (which are impractical to include here) reveal short-lived patches of size comparable to the correlation length that are ordered and aligned with the average image. We find that the times of relatively strong correlation are *not* dominated by regions where the local wave amplitude is small.

2. Circular symmetry

Measurements of $G_{IA}(t)$ for a circular cell are shown in Fig. 10(b). The calculation is again performed over the central quarter of the cell area. As in the square cell, the correlation coefficient exhibits approximately Gaussian

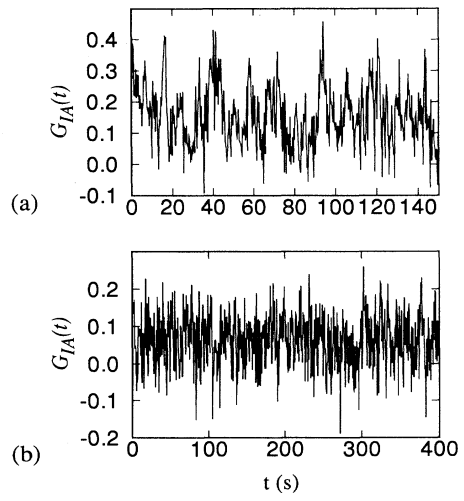

FIG. 10. Cross correlation coefficient $G_{IA}(t)$ between the instantaneous and average images as a function of time (a) for square cell B ($f_0=120$ Hz, $\varepsilon=1.5$, brim-full boundaries); (b) for circular cell C ($f_0=60$ Hz, $\varepsilon=1.00$). The fluctuations are approximately Gaussian; the instantaneous patterns never become fully ordered.

fluctuations, with no observed excursions above 0.3.

The symmetry of the averages in the *circular* cell suggests another useful function to investigate. Because the average image is azimuthally symmetric, i.e., $A(r,\theta)=A(r)$, it follows that

$$G_{IA}(t)\equiv\langle\delta A(r)\delta I(r,\theta)\rangle_{r,\theta}$$
$$=\int r\,dr\,\delta A(r)\langle\delta I(r,\theta)\rangle_{\theta}\ . \tag{4.4}$$

Therefore, in addition to inspecting the time- and space-dependent function $\delta A(\vec{x})\delta I(\vec{x},t)$, in the circular cell we look at the azimuthal average of the instantaneous image, $I_\theta(r,t)\equiv\langle\delta I(r,\theta)\rangle_\theta$. The function $I_\theta(r,t)$ is shown in Fig. 11, along with the corresponding radial variation of the time-averaged image, $A(r)$, for the images shown in Figs. 7(b) and 7(c). Note that the two functions show oscillations of similar shape and amplitude. However, the maxima do not line up perfectly. The amplitude and the phase of $I_\theta(r,t)$ are important in accounting for the behavior of $G_{IA}(t)$. Also notice that the instantaneous image [Fig. 7(b)] does not have obvious ring structure, despite the structure seen in its azimuthal average. Instead, the instantaneous image is made up locally of patches of square patterns.

To explore the time dependence of the correlations for the circular cell, we show in Fig. 12(a) an intensity coded plot of $I_\theta(r,t)$ for a series of instantaneous images, along with the corresponding measurement of $G_{IA}(t)$. Distinct vertical bands, corresponding to the time average images, can be observed by viewing the images at a glancing angle. The bands fade in and out as a function of time, and rarely seem to extend across the full radius of the cell. We observe that the corresponding value of $G_{IA}(t)$ increases at times when the vertical bands are prominent. At most times when the bands are strong, they are aligned in such a way as to contribute coherently to the average.

The same functions $I_\theta(r,t)$ and $G_{IA}(t)$ are shown for stronger excitation, $\varepsilon=1.00$, in Fig. 12(b). In this case, we observe that the vertical bands in $I_\theta(r,t)$ are much less apparent, and persist locally for much shorter times. The corresponding measurement of $G_{IA}(t)$ reveals fluctuations that are now much larger than the very small mean value; the characteristic time scale is also much reduced.

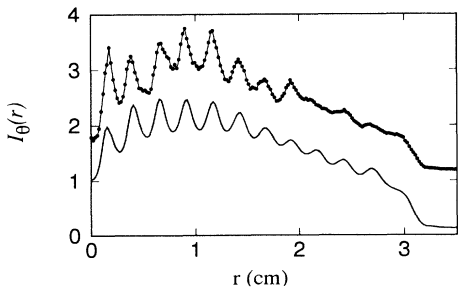

FIG. 11. Azimuthal averages of the instantaneous image (line with dots, offset) and time-averaged image (solid line) for circular cell C ($f_0=81$ Hz, $\varepsilon=0.50$). The data correspond to the images shown in Figs. 7(b) and 7(c).

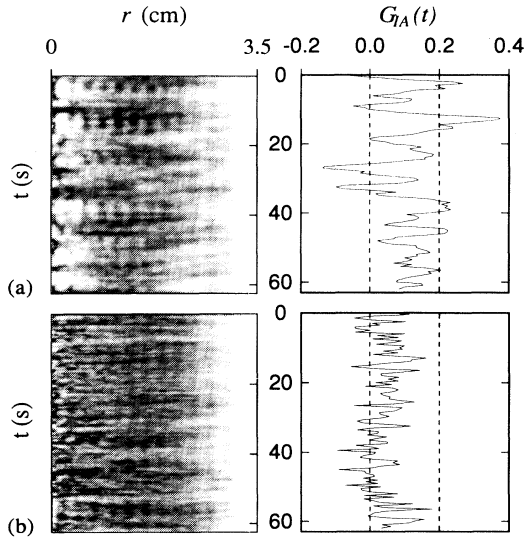

FIG. 12. Intensity-coded plot of the azimuthally averaged instantaneous images as a function of radius and time, and the corresponding cross correlation coefficient $G_{IA}(t)$ at (a) $\varepsilon=0.5$ and (b) $\varepsilon=1.0$. The data are from the circular cell C, $f_0=81$ Hz. When symmetric patches appear in the azimuthal average, they are phase coherent with the average.

The structure in the time-averaged image is still quite evident.

These studies of time-dependent correlations indicate that the structured averages are a consequence of phase coherence that is induced in the instantaneous wave patterns by the boundaries.

C. Approach to the mean

Finally, we ask the rather simple question of how the time averages converge, as the averaging time is increased. In order to address this issue, we measure the rms difference between finite and infinite time averages:

$$F(\tau)=\langle(A(\vec{x},\tau)-A(\vec{x},\infty))^2\rangle^{1/2}\ , \tag{4.5a}$$

where

$$A(\vec{x},\tau)=(1/\tau)\int_0^\tau I(\vec{x},t)dt\ . \tag{4.5b}$$

For a system with random Gaussian fluctuations, this function would decay as the inverse square root of the integration time. Typical measurements of $F(\tau)$ are shown in Fig. 13 on logarithmic scales for three different drive amplitudes. For each ε, the result is approximately a power law; the magnitude of the average exponent is 0.40 ± 0.03, clearly below 0.5. A broken line is drawn for reference with slope 0.4. (The exponents appear to fluctuate somewhat from run to run.) The fact that the magnitude of the slope is below 0.5 implies significant time correlations that decay more slowly than an exponential.

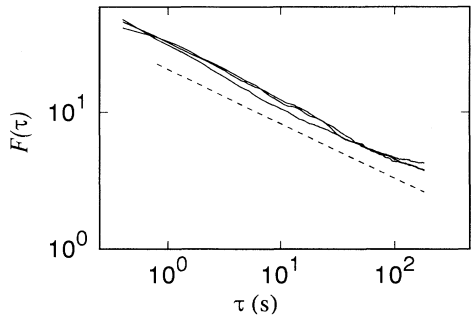

FIG. 13. Rms deviation of the short time average from an infinite time average, as a function of integration time (circular cell C; $f_0=60$ Hz; $\varepsilon=0.75$, 1.00, 1.25). The slope of the dashed line is -0.4.

V. INTERPRETATION OF TIME-AVERAGED IMAGES

In this section we address the problem of interpreting images that have been averaged over a time *long* compared to the characteristic time of fluctuations. We show that the averaged image is related to the probability distribution function (PDF) of spatial phase fluctuations of the underlying wave pattern. This result follows qualitatively from the statement that the optics highlight only the extrema of the local instantaneous wave pattern. Therefore, the time average intensity at a particular position is proportional to the fraction of time that position is occupied by an antinode in the wave pattern.

In the following subsections, we develop interpretations for the time averages using several simple models. First, we consider a one-dimensional model incorporating phase fluctuations that vary slowly in space and we formally show how the rms power in the average pattern is related to the width of the PDF of local phase fluctuations. We then extend the model to two dimensions in Sec. V B. In the third and fourth subsections we consider wave number quantization effects, and the role of amplitude variations. Finally, we show the correspondence between the time average of *images* and the time average of the wave pattern.

A. One-dimensional model

Our imaging process is much more sensitive to phase fluctuations than it is to amplitude fluctuations. Therefore, we consider an idealized one-dimensional model for the spatial part of a standing wave with spatially and temporally varying phase, but constant amplitude:

$$\zeta(x,t)=a\cos(\kappa x+\varphi(x,t)) . \tag{5.1}$$

We now use the fact, justified in Sec. III B, that the recorded image is approximately a δ function of the local surface height *gradient*, $I(x,t)=I_0\delta(\beta(x,t))$, where

$$\beta(x,t)=\partial_x\zeta(x,t)\approx-\kappa a\sin(\kappa x+\varphi(x,t)) . \tag{5.2}$$

We have assumed that the phase gradient is small. This reduces the image essentially to a sum of δ functions:

$$I(x,t)=I_0\frac{1}{\kappa a}\sum_{n=-\infty}^{n=\infty}\delta(\kappa x+\varphi(x,t)-n\pi) . \tag{5.3}$$

In order to compute the time average of this function, $A(x)=\overline{I(x,t)}$, we introduce the PDF of the local phase fluctuation,

$$P(\varphi,x)\equiv\frac{1}{T}\int_0^T dt\,\delta(\varphi(x,t)-\varphi) , \tag{5.4}$$

normalized such that $\int d\varphi\,P(\varphi,x)=1$. It then follows that

$$A(x)=\frac{I_0}{N}\sum_n P(n\pi-\kappa x,x) , \tag{5.5}$$

where N is a constant. Therefore, the spatial dependence of the average image is related to the PDF of the local phase fluctuations. If the phase fluctuations were evenly distributed over the range $[-\pi,\pi]$, then the average image would be structureless. On the other hand, suppose that the phase fluctuations are Gaussian with a width σ independent of position,

$$P(\varphi)\propto\exp(-\phi^2/2\sigma^2) . \tag{5.6}$$

In this case, the average image will have structure. We insert this distribution into Eq. (5.5) and expand in a Fourier series. The average then becomes (apart from the normalization)

$$A(x)\propto 1+\sum_{m>0}e^{-2m^2\sigma^2}\cos(2m\kappa x) . \tag{5.7}$$

It is now easy to see that if the distribution is reasonably wide, e.g., $\sigma>\pi/4$, then the terms with $m>1$ can be neglected, and the resulting time average is approximately $1+\alpha\cos(2\kappa x)$, with $\alpha=\exp(-2\sigma^2)$. Note that the wave number of the average image is twice that of the base pattern. This results from imaging both the positive and negative extrema of the wave pattern. In this highly idealized case, the rms fluctuation in the average, normalized by its mean, is

$$\frac{\delta A_{\rm rms}}{\langle A\rangle}\equiv\frac{\langle[A(x)-\langle A(x)\rangle]^2\rangle^{1/2}}{\langle A(x)\rangle}=\frac{1}{\sqrt{2}}\exp(-2\sigma^2) , \tag{5.8}$$

where the brackets indicate spatial averages. This derivation is only weakly dependent on the assumed form of the PDF. Provided the distribution is symmetric and peaked, the result (5.8) can still be used to estimate the width σ from the rms fluctuation in the average, and the corrections will appear at the higher wave numbers.

To be useful for chaotic waves, this model must be extended to include possible gradual spatial variations of the PDF of phase fluctuations in (5.1)–(5.7). These variations can be manifest in two different ways: as spatial drifts in the average local phase, and as changes in the width of the distribution. The former affect the *positions* of the resulting maxima, while the latter result in local changes in *contrast*, or amplitude, of the measured averages. This separation can be seen by rewriting (5.1) as follows:

$$\zeta(x,t)=a\cos(\kappa x+\bar{\varphi}(x)+\varphi'(x,t)) , \tag{5.9}$$

where $\bar{\varphi}(x)$ is the average phase at x, and $\varphi'(x,t)$ is the local phase fluctuation. With the assumption that both the time average phase $\bar{\varphi}(x)$ and the width $\sigma(x)$ of the distribution of $\varphi'(x,t)$ are slowly varying functions of position, the resulting average image is

$$A(x)\propto 1+\alpha(x)\cos 2[\kappa x-\bar{\varphi}(x)] , \tag{5.10}$$

where $\alpha(x)=\exp[-2\sigma^2(x)]$. In summary, we have shown using a simple one-dimensional model that the time average image can be simply related to the PDF of phase fluctuations of a base pattern. The wave number of the average is *twice* that of the base pattern; its phase varies in space and is equal to twice the local average phase of the instantaneous pattern.

B. Two-dimensional model

The one-dimensional (1D) model of Sec. V A is relatively simple to generalize to two dimensions. We use the fact that the δ function can be separated as in (3.3). Theory predicts that the standing waves can be approximated as a superposition of waves in two orthogonal directions. Allowing phase fluctuations, we write the square pattern (2.2) in the form

$$\zeta(\vec{x},t)=a[\cos(\kappa x+\varphi_x(\vec{x},t))+\cos(\kappa y+\varphi_y(\vec{x},t))] . \tag{5.11}$$

We now introduce the *joint probability distribution* for the fluctuating phases

$$P(\varphi_x,\varphi_y,\vec{x})\equiv\frac{1}{T}\int_0^T dt\,\delta(\varphi_x(\vec{x},t)-\varphi_x)\delta(\varphi_y(\vec{x},t)-\varphi_y) . \tag{5.12}$$

The average pattern then becomes

$$A(\vec{x})=N^{-1}\sum_{n,m=-\infty}^{n,m=\infty}P(n\pi-\kappa x,m\pi-\kappa y,\vec{x}) . \tag{5.13}$$

In some cases, it is useful to average this function along one of the spatial dimensions, say y, to obtain

$$A_y(x)\equiv\langle A(\vec{x})\rangle_y=N^{-1}\sum_{n=-\infty}^{n=\infty}P_y(n\pi-\kappa x,x) , \tag{5.14}$$

where

$$P_y(\varphi,x)\equiv\sum_{m=-\infty}^{m=\infty}\langle P(\varphi,m\pi-\kappa y,x,y)\rangle_y . \tag{5.15}$$

This operation is applicable for the case where the orientation of the base pattern is essentially fixed, and there is no direct dependence between φ_x and φ_y. It is straightforward to show that the function $A_y(x)$ has the same form as (5.10), provided that P_y has a single maximum. Recall that a measurement of this function is shown in Fig. 6 for an average image in the square cell; the data are quite similar to (5.10). Therefore the interpretation of a two-dimensional time-averaged image, after averaging over one coordinate, is similar to that of a one-dimensional standing wave; the rms amplitude of the average is related to the variance of phase fluctuations. We shall use these results again in Sec. VI.

C. Fluctuations about multiple quantized states

It is also useful to consider what happens to the average image if the surface wave pattern alternates between states characterized by different mean wave numbers. For example, this might occur in a finite box of width L, where the boundaries impose a fixed phase at the walls, and therefore a quantized total phase difference between walls, but the number of half wavelengths switches between N and $N+1$. The resulting average image is a linear superposition of the individual average images for each of the two fluctuating states. In one dimension, the result is of the form

$$A(x)=P_N[1+\alpha_N\cos(2\kappa_N x)]+P_{N+1}[1+\alpha_{N+1}\cos(2\kappa_{N+1}x)] , \tag{5.16}$$

where P_N is the probability of being in state N. This expression easily reduces to

$$A(x)=1+A_N\cos(2\kappa_N x)+A_{N+1}\cos(2\kappa_{N+1}x) . \tag{5.17}$$

Because these two cosine terms are in phase at the walls (Neumann boundaries) and partially out of phase elsewhere, the rms amplitude of the average image varies as a function of position. *Thus one hallmark of a superposition would be a loss of contrast in the central region of the average image.*

D. Amplitude modulations

We have assumed in the previous models that phase fluctuations are important but that amplitude variations are not. This assumption is appropriate for our imaging system only if the local amplitude $a(x)$ is sufficiently large that $\kappa a(x)\gg\Lambda=0.026$. If the local amplitude does vanish, e.g., due to the presence of a defect, a corresponding bright spot appears in the image. This can be seen by reevaluating (5.2), allowing $a(x,t)=0$, but maintaining the assumption that $\partial_x a(x,t)$ is negligible. This assumption, while mathematically somewhat tenuous, is justified as a rough approximation because the bright areas in the image are observed to be larger than the spots produced by typical antinodes. Then (5.3) becomes

$$\frac{I(x,t)}{I_0}=\frac{\delta(a(x,t))}{|\kappa\sin(\kappa x+\varphi(x,t))|}+\frac{1}{\kappa a}\sum_{n=-\infty}^{n=\infty}\delta(\kappa x+\varphi(x,t)-n\pi) . \tag{5.18}$$

After time averaging this function, the first term in this equation gives a contribution to $A(x)$ proportional to the local probability that the amplitude goes to zero, while the second term can be analyzed as before. The resulting time average is a superposition of these two results. Because we have assumed that $\partial_x a$ is small, the first term contributes only a slowly varying background to $A(x)$, while the second term is responsible for most of the short

wavelength structure. Thus, amplitude modulations do not dramatically affect the structure of the time-averaged images.

E. Relation between the average image and the average wave pattern

In the preceding sections we showed that the structure in the time-averaged image is related to phase fluctuations of the instantaneous wave patterns, and is insensitive to amplitude fluctuations. However, our actual interest is in the statistics of the wave patterns themselves, not the images. We therefore consider the relation between the time-averaged images and the time average of the wave function ζ, the wave height stroboscopically measured at constant phase with respect to the drive. It is relatively straightforward to show that the time average of (5.9) is

$$\overline{\zeta(x)}=a\int d\varphi\, P(\varphi,x)\cos[\kappa x+\bar{\varphi}(x)+\varphi]\ . \tag{5.19}$$

If we assume that $P(\varphi,x)$ is a symmetric (even) function of φ, this reduces to the form

$$\overline{\zeta(x)}=\psi(x)\cos[\kappa x+\bar{\varphi}(x)]\ , \tag{5.20}$$

where $\psi(x)=a\int d\varphi\, P(\varphi,x)\cos(\varphi)$. [An asymmetric portion of the distribution would add a negative second term in (5.20) with both cosines replaced by sines.] A fluctuating amplitude $a(x,t)$, as considered in Sec. V D could also be incorporated, and would yield the result that $\psi(x)=a(x)\int d\varphi\, P(\varphi,x)\cos(\varphi)$, provided that the fluctuations in amplitude and phase are statistically independent.

If we now compare $\overline{\zeta(x)}$ to $A(x)$ in (5.10), we observe that the two functions are very similar: both have an oscillation amplitude that is a function of the PDF of the phase fluctuations. The amplitude *decreases* with the width of the PDF in both cases. The wave numbers and phases of the two functions differ by exactly a factor of 2. Furthermore, *we conclude that the observation of structured time-averaged images implies structure in the average wave pattern.* The structured averages are not due to artifacts of the imaging technique.

F. Summary

We have shown in Sec. V that the average image can be interpreted in terms of the probability distribution of phase fluctuations about a base wave pattern; amplitude variations of the waves are not important for interpreting the average images. The wave number of the average image is equal to twice the mean wave number of the base pattern, in both one and two dimensions. The local amplitude of the average image is related to the variance of the local phase fluctuations. Phase drifts in the average image reflect spatial variations in the mean phase. In addition, we have shown that if the wave number is statistically quantized, and if several states occur with significant probability, the resulting average image is a superposition of averages about the individual states. Finally, structure in the average *image* implies structure in the average surface *wave pattern.* These results are central to our interpretation of the further experimental results contained in Sec. VI.

VI. EXPERIMENTS: DEPENDENCE ON PARAMETERS

In this section, we investigate the systematics of the time averages as a function of various drive parameters in the square and circular cells. We use these statistics, within the context of the models presented in Sec. V, to develop an understanding of the *instantaneous* patterns. We start by investigating the variation of the average pattern as a function of drive amplitude and boundary conditions. Next, we discuss the response observed in the average images to variations of the drive frequency. The average images have a distinct wave number that is related to the mean wave number of the instantaneous wave patterns. [This is also not far from the wave number of the Faraday instability at lower ε, as specified in (2.1).] By varying the drive frequency and therefore the mean wave number of the instantaneous patterns, we probe the wave number selection process for the average images. We describe the phenomena separately for square and circular geometries in sections VI B and VI C since they need to be modeled somewhat differently.

A. Drive amplitude and boundary conditions

As the drive acceleration is increased, the instantaneous patterns become more strongly disordered, and the time scale for fluctuations decreases [6,22]. As we explained in Sec. V A, the rms amplitude of the average images is related to the rms width of the distribution of phase fluctuations. Therefore, one might expect the amplitude of the averages to decrease as ε is increased; this is in fact what we find. Figure 14(a) shows the rms amplitude of average images in a circular cell as a function of ε for two different drive frequencies, $f_0=60$ and $f_0=120$ Hz:

$$\delta A_{\rm rms}\equiv\langle(A(\vec{x})-\langle A(\vec{x})\rangle)^2\rangle^{1/2}\ . \tag{6.1}$$

The measurements are performed at constant frequency. After each increment of the drive amplitude, we acquire a series of 10 instantaneous images and a time average. In order to minimize effects due to the radial nonuniformity of the illumination, we calculate $\delta A_{\rm rms}$ only over the central region of the image, and filter out contributions from very low wave numbers in Fourier space. As is suggested by (5.8), we normalize the rms amplitude by the average intensity in the central region.

The amplitude of the average images decreases monotonically with increasing drive amplitude. The corresponding aspect ratios for these two drive frequencies are 10 and 17, respectively. We attribute the more rapid decline of the amplitude at the higher frequency to the larger aspect ratio. Even at the highest drive amplitudes shown here, structure is discernible. Somewhat beyond this range ($\varepsilon\sim 3$), droplets begin to break off from the fluid surface, so it is impractical to extend the measurements further.

We have performed similar experiments with the smaller square cavity, cell B, with both wetting and brim full boundary conditions. The results, shown in Fig. 14(b) for $f_0=120$ Hz, reveal that the power in the average images decreases as a function of drive amplitude, as in the circular cell. In addition, we find that brim-full boundary condition leads to a stronger average. This result can be understood as a consequence of increased pinning of the phase of the waves at the boundaries, where the $\zeta=0$. This situation is in contrast to the flexible boundary conditions associated with the meniscus in the wetted case, where the width and mean height of the meniscus can more easily fluctuate. We note that, with a literal interpretation of (5.8), the observed range $0.01 \leq \delta A_{\rm rms}/\langle A \rangle \leq 0.2$ would correspond to $0.46 \geq \sigma/\pi \geq 0.25$.

We have also tested the case of over-full boundary conditions [Fig. 2(b)] in the smaller square cell. In this geometry, traveling waves are free to propagate outward beyond the boundaries, where they are strongly damped. Although the instantaneous images have features similar to those observed with other wetting conditions, the structure in the average images is barely distinguishable over the noise level, and is close to being azimuthally symmetric. In summary, the strength of the average image decreases with increasing disorder (or phase fluctuations), and depends on the degree of phase pinning at the boundaries.

B. Frequency dependence in the square geometry

By varying the drive frequency, we can explore the nature of the pattern fluctuations. In this section, we describe the amplitude and wave number of the average images as a function of frequency for a square cell, and supplement these measurements with spectral data. We interpret the results in terms of the models of Sec. V.

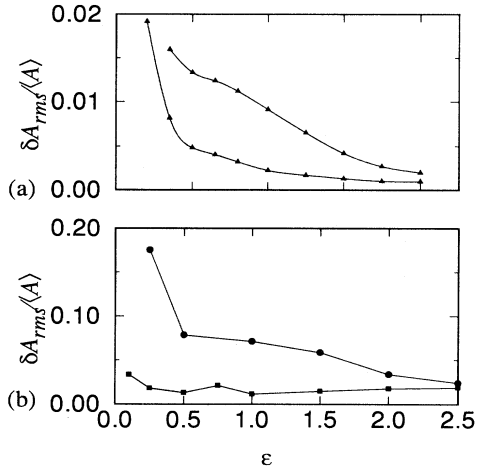

FIG. 14. Amplitude (rms) of the average images as a function of drive amplitude. (a) Circular cell C at $f_0=60$ Hz (upper curve) and $f_0=120$ Hz (lower curve); (b) square cell B at $f_0=120$ Hz. Symbols: wetting boundaries (squares); brim-full boundaries (circles). The amplitude declines as the variance of the phase fluctuations increases.

1. Experimental observations: Amplitude and wave number

The amplitude $\delta A_{\rm rms}$ of the average image as a function of drive frequency is shown in Fig. 15(a) for square cell A. The data are taken by incrementing both the frequency and drive amplitude in order to maintain a constant nondimensional drive amplitude corresponding to $\varepsilon=1.0$. A distinct oscillation in the amplitude of this function is observed. The corresponding wave number q for the average image, shown in Fig. 15(b), is observed to have jumps at the same drive frequencies as the depressions in the amplitude of the average image. Both the amplitude and wave number are calculated for the central region of the cell. The wave number predicted from linear stability theory for onset patterns in an infinite system is shown as a solid line.

The wave number measurements were made using Fourier methods [34] applied to the central region $L/4<x,y<3L/4$ of the cell. We nondimensionalize the resulting wave number by dividing by $2\pi/L$, where L is the width of the cell. The result is the (possibly nonintegral) number of periods of the average image in an interval of length L. Within the context of the models presented in Sec. V, this number is equal to the number of *half* wavelengths of the base pattern describing the fluid height.

The difference between peak nondimensional wave numbers for consecutive steps is almost exactly unity. Because the nondimensional wave number is equal to the number of half wavelengths of the base pattern, we conclude that the observed discreteness is related to mode pulling of the pattern by the box size, i.e., an effective box quantization of the base pattern. For true quantization, the quantity $qL/2\pi$ should be constant between the jumps. However, it actually *decreases* between jumps by almost a full integer. This is curious because the wave number predicted by linear stability (which of course only applies near onset) monotonically *increases* with frequency.

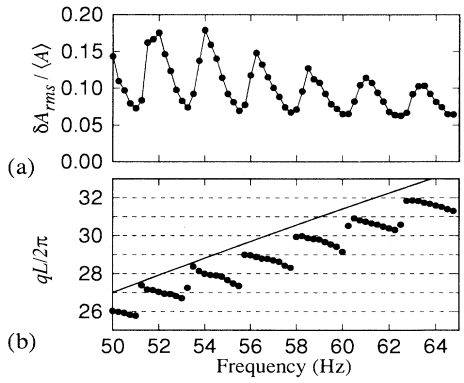

FIG. 15. Frequency dependence of (a) the amplitude and (b) the nondimensional wave number of the average image (square cell A, $\varepsilon=1.0$), calculated over the central region, $L/4<x,y<3L/4$, of the cell. The solid line in (b) is the wave number predicted by the dispersion relation. Jumps in q correspond to quantization of the base pattern.

2. Discussion

We pause now to consider the frequency dependence of q within the context of the 1D analysis presented in Secs. V A and V C. The first question we must address is whether the average images are simply due to fluctuations about a single quantized state, as described by (5.10), or whether they result from fluctuations about two different quantized states, as described by (5.17). The answer turns out to depend on the drive frequency. In the latter case, the two waves would be in phase near the walls, and would be out of phase in the center, resulting in a relative *decrease* in contrast of the average near the center of the cell.

Let us first consider the situation at frequencies between the jumps. We found that the amplitude of the measured averages is nearly constant over the width of the cell. This excludes the two-state situation from being applicable here. Therefore, *between the wave number jumps, the surface is primarily fluctuating about a single quantized base state.*

Next, we must account for the variation of the wave number between the jumps. Two possibilities present themselves: either the effective width of the box changes, or the wave number is spatially nonuniform. The former could occur if the width of the meniscus varies with f_0. We estimate how much the width of the meniscus would vary by calculating the effective size L_{eff} of the box under the assumption that the wave number is actually quantized, $qL_{\text{eff}}/2\pi = n$. The resulting peak-to-peak deviation corresponds to an effective change in the box size of approximately 4 mm. The typical width of a single meniscus, given by $l \sim \sqrt{\gamma/\rho g}$, is approximately 2 mm, so that this effect is probably not large enough to account for the wave number variation along the steps.

The variation of the wave number between the jumps must therefore be explained by a spatially varying wave number. Within the context of the model (5.10), this would correspond to a spatially varying mean phase, $\bar{\varphi}(x)$. We have measured q in the central region of the average image, and we assumed that $\bar{\varphi}(x)$ is constant in that region. In order to look for spatial variations of q, we measure the *local* wavelengths of the average image as a function of position in the cell. The method used is simply to find the distance between neighboring maxima of the function $A_y(\vec{x})$. We observe that, at some frequencies, the wavelength near the boundaries of the cell is as much as 20% *larger* than it is in the central region of the cell; the local wavelength decreases steadily over the first 3–5 periods from the wall, and remains fairly constant in the central region. As a function of frequency, the wavelength near the boundaries *decreases* [between the jumps in Fig. 15(b)]. These observations are consistent with the conclusion that *the total number of periods of the average across the cell is quantized between the jumps;* the apparent gradual change in q in the central region is compensated by an opposite variation near the walls.

We have argued that in the regions between the jumps in Fig. 15(b), the average image can be modeled as resulting from a single-wave number state plus phase fluctuations, as in (5.9). We now ask the question: what is the nature of the sharp transitions or jumps in the wave number? Close to the transition, does the surface fluctuate about two different states? If so, does the pattern stay on one of these two attractors until it discontinuously jumps to the other? Or are the dynamics better described by orbits of varying length about each state, with the relative probability of being in one state or the other varying continuously with drive frequency?

In order to probe these questions, we show in Fig. 16(a) a high resolution measurement of the wave number as a function of increasing and decreasing frequency, while maintaining constant drive amplitude ε. The results follow one *nonhysteretic,* continuous curve. In addition, we have measured the wave number over the same range, but reducing the drive amplitude to zero before changing frequency. The resulting measured wave numbers again fall on the same curve. The amplitudes of the resulting averages (not shown) are consistent with those observed in Fig. 15(a); the rms amplitude decreases at the frequencies for which the measured wave number increases sharply. Visually, the amplitude declines most strongly near the center of the cell at frequencies coincident with the jump in wave number. This loss of contrast is illustrated in Fig. 16(b), which displays the vertical average $A_y(x, f_0)$ for this range of frequencies. *These results are consistent with the two-state model (5.17) for the regions within the jumps,* where the probability of being in one state or the other varies continuously with drive frequency.

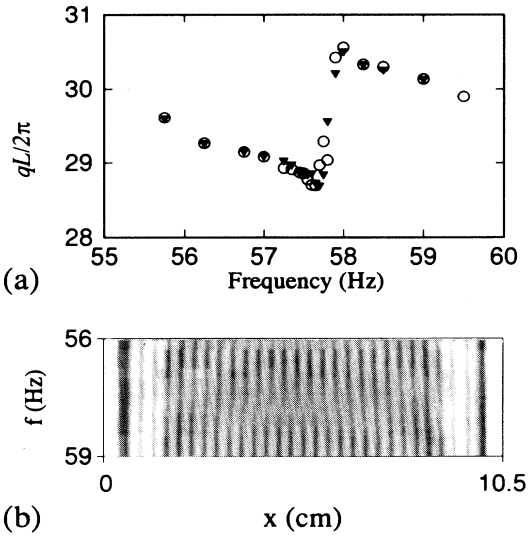

FIG. 16. (a) High resolution measurement of the mean wave number as a function of drive frequency near a wave number jump (square cell A, $\varepsilon = 1.0$) calculated over the central region of the cell, $L/4 < x,y < 3L/4$. The symbols correspond to increasing frequency (circles) and decreasing frequency (triangles). No hysteresis is observed. (b) Intensity coded plot of the y average of time-averaged images as a function of drive frequency, for the same data as in (a). The contrast decreases at the center of the cell for frequencies coincident with the observed jump in wave number.

3. *Experimental observations: Orientational fluctuations*

Additional information about the instantaneous patterns in the square cell can be derived from the spatial power spectrum of the instantaneous images, which reveals the degree of orientational order of the instantaneous wave pattern. The ensemble average of the power spectrum shows the range of orientations of ordered patches in the instantaneous patterns. Power spectra of instantaneous images are shown at two frequencies in Figs. 17(a) and 17(b). We have averaged the spectra over 30 images. The data are from the same run as Fig. 16, and the two frequencies are chosen to correspond to the region within a jump in wave number [Fig. 17(a)] and a region between jumps [Fig. 17(b)]. The spectra are calculated over the central region of the measured patterns, and are shown logarithmically using a gray scale.

Most of the spectral power is distributed over an annulus, as found earlier by Tuffillaro, Ramshankar, and Gollub [6]. However, the angular distribution varies with frequency, and is much more evenly distributed in Fig. 17(a) than in Fig. 17(b). To quantify this effect, we determine the rms variation of power $\delta P_{\rm rms}$ on an annulus centered around the peak wave number, normalized by the total power $\langle P \rangle_\theta$. This function is a measure of the range of orientations of the ordered patches in the instantaneous images. Figure 18 shows $\delta P_{\rm rms}$ as a function of drive frequency, for the same data run as Fig. 16.

The minima of $\delta P_{\rm rms}$ occur at the same drive frequencies as the jumps in wave number of the average pattern. From this measurement we infer that the instantaneous wave patterns are preferentially aligned with the cell

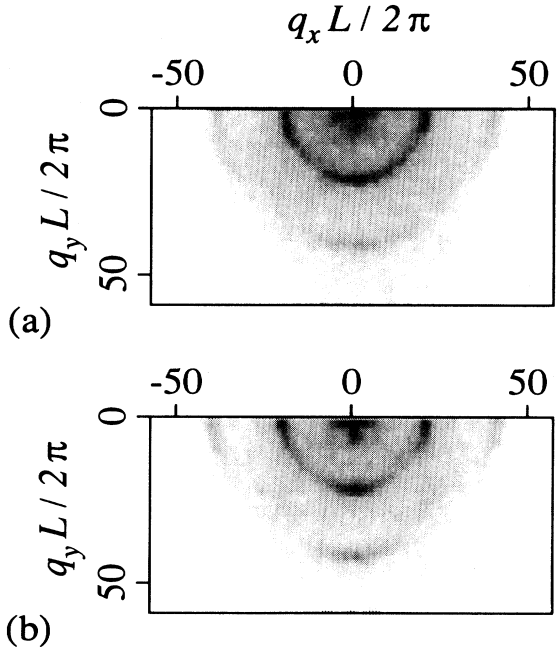

FIG. 17. Wave number spectra of instantaneous images at (a) $f_0 = 57.75$ Hz and (b) $f_0 = 58.5$ Hz in square cell A. The angular distribution is more uniform in case (a), coincident with the jump in the wave number (see Fig. 16).

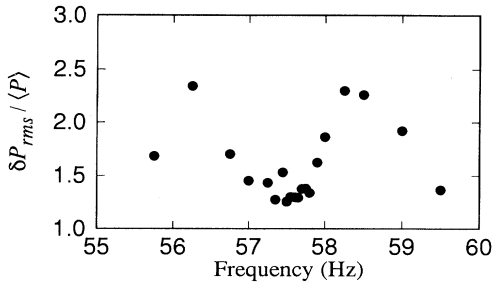

FIG. 18. Azimuthal anisotropy in the spectral power as a function of frequency in square cell A, for the same range as Fig. 16. The minimum in $\delta P_{\rm rms}$ occurs at the same frequency as the wave number jump, and indicates enhanced orientational fluctuations.

walls at drive frequencies between the jumps in wave number where a single wave number model is applicable, and are more randomly oriented at the frequencies for which a two state model is needed. This suggests that *the largest variations in orientation are associated with transitions between different base states* of the instantaneous pattern.

4. *Summary*

In summary, well-defined jumps in the wave number of the average images occur as a function of drive frequency. The measurements and observations lead to the following general picture of the pattern fluctuations. The jumps correspond to integral changes of the total phase difference of the base pattern across the cell. However, the local wave number varies with position. The instantaneous patterns can be described as fluctuating either about a single quantized state, or about two quantized states with different wave numbers (as in Sec. V C), depending on the drive frequency. The orientational fluctuations are enhanced in the latter situation.

C. Frequency dependence in the circular geometry

1. *Experimental Observations: Amplitude and wave number*

We have also investigated the frequency dependence of the average images in the circular cell. As we found for the square cell, the amplitude of the averages [Fig. 19(a)] oscillates; it also declines with increasing frequency, i.e., increasing aspect ratio. One may infer that the structure would fade out completely for sufficiently high aspect ratio, as it does for sufficiently high excitation amplitude.

The wave number q of the average image [Fig. 19(b)] displays jumps for the circular cell as a function of drive frequency, as well as a marked downward slope between the jumps. For the circular cell data, we measure the wave number from the radial dependence of the average pattern in real space, instead of using Fourier methods. We nondimensionalize by $2\pi/D$, where D is the cell diameter. The jumps in wave number coincide with the local minima in Fig. 19(a). The spacing of the jumps is

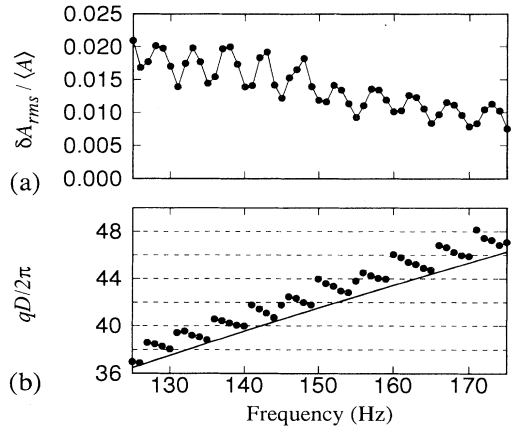

FIG. 19. Frequency dependence of (a) the amplitude and (b) the nondimensional wave number of the average image (circular cell C, $\varepsilon=0.5$) calculated over the central region, $r<3R/4$, of the cell. The solid line in (b) is the wave number predicted by the dispersion relation.

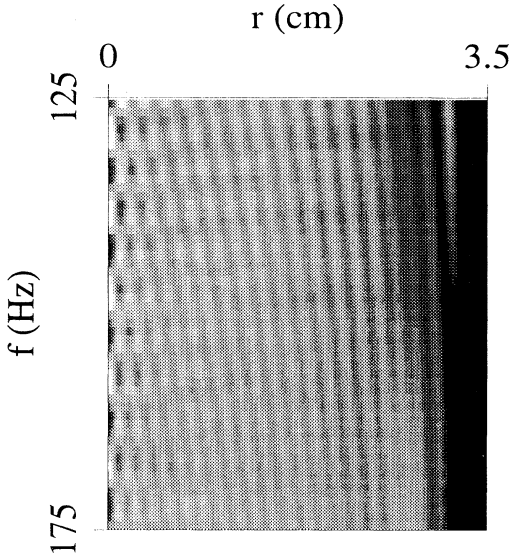

FIG. 20. Intensity coded plot of the average image in circular cell C as a function of radius and drive frequency (same data as Fig. 19). The average at the center of the cell can be a local maximum or a minimum, depending on frequency.

again consistent with an effective box quantization. In contrast to the data observed in the square cell, the measured wave number falls consistently *above* that predicted by the dispersion relation.

2. Discussion

The quantity $qD/2\pi$ in the circular case is approximately equal to the number of periods in the average across the diameter of the cell. As for the square cells, it is useful to consider the average image as resulting from a simple base wave pattern with phase fluctuations. We now consider the nature of the base wave patterns about which the instantaneous patterns fluctuate: Are they normal modes of the container, $S_n(r,\theta)=J_n(kr)\cos n(\theta-\theta_n)$, composed of Bessel functions in the radial direction and the corresponding angular factors? Or are they square-symmetric waves, as would occur in the infinite plane near onset? We show below that the square-symmetric waves provide a better model even in the circular geometry.

To determine which approach is superior, we note that for the simplest Bessel mode pattern, S_0, the appropriate quantization condition would involve the number of half wavelengths across the *radius* of the cell. In addition, the center would always contain a local maximum (even when fluctuations are included). The only Bessel mode which could result in a local minimum at the center of the average would be S_1. Higher order circular modes all have zero amplitude and zero slope at their centers, and would therefore also produce local intensity maxima at their centers. In Fig. 20 we show an intensity coded plot of the average image, azimuthally averaged, as a function of radius and frequency. By looking down along the left side of this plot (i.e., at $r=0$) we observe that the average intensity at the center of the cell oscillates as a function of frequency, and is sometimes a relative *minimum* with respect to r. Therefore a Bessel mode description would require that S_1 be included at some frequencies. On the other hand, the instantaneous images all display patches of local fourfold symmetric patterns which would require higher order modes. Therefore a description in terms of Bessel modes would be fairly complex.

We now show that the results of Figs. 19 and 20 are consistent with a model based on square symmetric waves plus phase and orientational fluctuations. We focus attention initially on a single wave number base pattern at one orientation and later average over angles. Appropriate base patterns take one of the following three forms:

$$\begin{aligned}\zeta_+ &= \cos(\kappa x'+\varphi_{x'})\pm\cos(\kappa y'+\varphi_{y'})\ ,\\ \zeta_0 &= \cos(\kappa x'+\varphi_{x'})\pm\sin(\kappa y'+\varphi_{y'})\ ,\\ \zeta_- &= \sin(\kappa x'+\varphi_{x'})\pm\sin(\kappa y'+\varphi_{y'})\ .\end{aligned}\tag{6.2}$$

We have chosen the origin at the center of the cell, and the primes denote a reference frame at an angle Υ with respect to the x,y axes; these patterns are aligned with respect to the x',y' axes. The average image *while aligned in this way* can be calculated by following the arguments of Sec. V B. We expect that the boundaries will impose a reflection symmetry after averaging over phase fluctuations, i.e., $\varphi_{x'}(x')=\varphi_{x'}(-x')$, and $\varphi_{x'}(0)=0$. Because of the full rotational symmetry of the cell, Υ also fluctuates; these angular fluctuation should be statistically independent of the fluctuations in phase. Therefore, we also average over Υ. The result is $A(r)=1\pm aJ_0(2\kappa r)$ for ζ_+ and ζ_- and $A(r)=1$ for ζ_0. This model allows either a maximum or minimum at the center, and displays rings approximately evenly spaced radially. It is therefore qualitatively compatible with the observations. However, experimental limitations appear to preclude further quantitative tests.

3. *Summary*

In summary, in order to account for the observed average images in the circular cell, a description of the instantaneous patterns based on Bessel modes would be excessively complex. A simpler description may be constructed using fluctuating square-symmetric waves (2.2), with rotational freedom about a fixed origin. This description coincides with the visual appearance of the instantaneous patterns [Fig. 7(b)] and with the patterns expected in an infinite layer.

VII. SUMMARY AND CONCLUSIONS

The most striking observation of this investigation is that structure is found in the time-averaged images of chaotic wave patterns. The imaging process essentially highlights the antinodes of the wave patterns; the time-averaged images can therefore be interpreted in terms of the probability density of antinode positions, which in turn is related to the local distribution of phase fluctuations of the pattern. Structure in these averages implies long range phase coherence and a constrained phase at the boundaries. The symmetry of the observed structure is then determined by the boundaries, not by the symmetry of the fluctuating pattern. Quantization effects are observed in the averaged images as the wave number of the pattern is varied.

We have investigated chaotic wave patterns as a function of container geometry, boundary wetting, drive frequency and drive amplitude. Through careful consideration of the imaging process, we show how measurements of averaged quantities can be interpreted to reveal detailed information about the instantaneous patterns. The main results are as follows.

(i) Time-averaged shadowgraph images can be interpreted in terms of a simple model for the instantaneous waves based on local phase and amplitude fluctuations about a single wave number base pattern. Both one- and two-dimensional versions of the model are described. The measurements are more sensitive to phase than to amplitude fluctuations. Structure in the time averaged shadowgraph image implies structure in the time average of the wave pattern.

(ii) Spatially and temporally disordered surface waves at moderately high aspect ratio can have structured time-averaged patterns (Figs. 1 and 7–9). The symmetry of the average patterns is determined by the symmetry of the boundaries, despite the fact that the instantaneous patterns are similar: they contain square-symmetric patches of locally ordered waves interspersed with defects. The structured averages imply that the distributions of phase fluctuations about the base pattern are peaked; the phase of the based pattern is fixed with respect to the boundaries. The most useful base pattern for both square and circular cells is a sum of sines (or cosines) for the fluid and parameters investigated; an additional rotational degree of freedom is needed for the circular cell. This base pattern is the same wave pattern expected near onset in an infinite plane.

(iii) The time-dependent cross correlation coefficient $G_{IA}(t)$ between an instantaneous image and the time average is a useful tool for probing the proximity of the instantaneous image to the average (Figs. 10 and 12). It reveals that the system continually fluctuates about the mean, but never becomes fully ordered. In phase space, the system should be viewed as fluctuating far from the fully ordered base state.

(iv) The convergence of the averaging process (Fig. 13) is significantly slower than that of a simple Gaussian process. This is indicative of time correlations that decay more slowly than an exponential function.

(v) The amplitude of an average pattern is sensitive to the degree of pinning of the meniscus at the boundaries [Fig. 14(b)]. The strongest structured averages are found when the meniscus is pinned by the corner of a ledge, whereas no structure is observed when the waves can propagate beyond the ledge.

(vi) The amplitude of the average image is a decreasing function of the degree of disorder in the instantaneous pattern; as the drive amplitude is increased, the contrast in the average images decreases (Fig. 14). This change corresponds to an increased variance in the local phase fluctuations. For sufficiently strong disorder, structured averages are undetectable.

(vii) The mean wave number of the average images is observed to have nonhysteretic jumps as a function of drive frequency (Figs. 15, 16, and 19). This phenomenon corresponds to integral changes of the total phase difference of the base pattern across the cell. The patterns observed at frequencies *between* the jumps are characterized by fluctuations about a single wave number state; for frequencies near the jumps, the patterns fluctuate about two states with different wave numbers.

(viii) The average orientation of instantaneous patterns in the square cell is biased by the walls of the container. The degree of angular bias, measured from the ensemble average of the spatial power spectra, is a function of drive frequency (Figs. 17 and 18). The largest orientational variations occur under conditions for which a two state model is appropriate; this observation suggests that large orientational deviations may be associated with transitions between the states.

We did not detect the symmetry-changing bifurcations described in Refs. [8–10], though we made some efforts to look for them. Rather, the time averages have the maximum symmetry allowed by the boundaries at all values of the excitation. It is of course possible that transitions might be found at lower excitation frequency (longer wavelength) or for other geometries. We did some additional experiments with an isosceles triangular cell, but the average patterns were difficult to interpret. In any case, many of the phenomena noted in this investigation could not have been anticipated based on symmetry arguments alone.

In the Introduction, we posed the question of how the averages might be related to nonchaotic wave patterns near onset, which are modes of the container at these aspect ratios. In general, there seems to be no deep connection. Instead, the averages are related to fluctuations about square-symmetric base patterns. For example, the ring structure in the time-averaged image for the circular cell arises naturally from the angular averaging over

wave patches with fourfold symmetry, in conjunction with phase pinning by the boundaries, and not from the Bessel function structure of the linear modes near onset.

Taken together, these measurements provide a number of ways of characterizing the spatiotemporal chaos. Similar methods could be used for other spatially extended systems. One significant result is the clear indication of residual phase coherence in a relatively large system. Similar results were found in rotating convection [12], so the phenomena are not uncommon, though the special properties of the Faraday system at low viscosity may allow the structured averages to be observed at higher aspect ratio. We showed that the instantaneous waves can be modeled as amplitude and phase fluctuations about a base state with a dominant wave number (or in some cases, two such states); the form of this base state is the one expected near onset in an infinite system (2.2).

These underlying states may be conceptually analogous to the coherent structures found in a variety of turbulent fluid systems [35–37]. Their presence suggests that the number of degrees of freedom of these extended systems may be smaller than one might have expected. The methods of proper orthogonal decomposition [35,38,39] could possibly be used as an alternate way of detecting what we have termed the "underlying base states" in this paper.

ACKNOWLEDGMENTS

We thank M. Golubitsky for suggestions which led us to begin this investigation. This work was supported by the National Science Foundation under Grant No. DMR-9319973, with initial support from Grant No. CTS-9115005.

[1] M. C. Cross and P. C. Hohenberg, Rev. Mod. Phys. **65**, 851 (1993).
[2] H. D. I. Abarbanel, R. Brown, J. J. Sidorowich and L. S. Tsimring, Rev. Mod. Phys. **65**, 1331 (1993).
[3] G. Ahlers and R. P. Behringer, Prog. Theor. Phys. Suppl. **64**, 186 (1978).
[4] I. Rehberg, S. Rasenat, and V. Steinberg, Phys. Rev. Lett. **62**, 756 (1989).
[5] E. Braun, S. Rasenat, and V. Steinberg, Europhys. Lett. **15**, 597 (1991).
[6] N. B. Tufillaro, R. Ramshankar, and J. P. Gollub, Phys. Rev. Lett. **62**, 422 (1989).
[7] S. W. Morris, E. Bodenschatz, D. S. Cannell, and G. Ahlers, Phys. Rev. Lett. **13**, 2026 (1993).
[8] M. Dellnitz, M. Golubitsky, and I. Melbourne, in *Bifurcation and Symmetry,* edited by E. Allgower, K. Bohmer, and M. Golubitsky (Birkhauser, Basel, 1992), p. 99.
[9] P. Chossat and M. Golubitsky, Physica D **32**, 423 (1988).
[10] M. Dellnitz, M. Golubitsky, and I. Melbourne, Arch. Rat. Mech. Anal. **123**, 75 (1993).
[11] B. J. Gluckman, P. Marcq, J. Bridger, and J. P. Gollub, Phys. Rev. Lett. **71**, 2034 (1993).
[12] L. Ning, Y. Hu, R. E. Ecke, and G. Ahlers, Phys. Rev. Lett. **71**, 2216 (1993).
[13] M. Faraday, Philos. Trans. R. Soc. London **225**, 298 (1831).
[14] T. B. Benjamin and F. Ursell, Proc. R. Soc. London, Ser. A **225**, 505 (1954).
[15] S. T. Milner, J. Fluid Mech. **225**, 81 (1991); W. Zhang and J. Vinals (private communication).
[16] A. B. Ezerskii, M. I. Rabinovich, V. P. Reutov, and I. M. Starobinets, Zh. Eksp. Teor. Fiz. **91**, 2070 (1986) [Sov. Phys. JETP **64**, 1228 (1986)].
[17] J. Miles and D. Henderson, Ann. Rev. Fluid Mech. **22**, 143 (1990).
[18] S. Douady and S. Fauve, Europhys. Lett. **6**, 221 (1988).
[19] S. Douady, J. Fluid Mech. **221**, 383 (1990).
[20] A. B. Ezersky and P. A. Matusov, Phys. Lett. A **170**, 48 (1992).
[21] A. B. Ezersky, S. V. Kiyashko, P. A. Matusov, and M. I. Rabinovich, Europhys. Lett. **26**, 183 (1994).
[22] J. P. Gollub and R. Ramshankar, in *New Perspectives in Turbulence,* edited by L. Sirovich (Springer-Verlag, New York, 1991), p. 165.
[23] W. S. Edwards and S. Fauve, J. Fluid Mech. **278**, 123 (1994).
[24] S. Ciliberto, S. Douady, and S. Fauve, Europhys. Lett. **15**, 23 (1991).
[25] V. S. Afraimovich, A. B. Ezersky, M. I. Rabinovich, M. A. Shereshevsky, and A. L. Zheleznyak, Physica D **58**, 331 (1992).
[26] E. Bosch and W. van de Water, Phys. Rev. Lett. **70**, 3420 (1993).
[27] E. Bosch, H. Lambermont, and W. van de Water, Phys. Rev. E **49**, R3580 (1994).
[28] R. Ramshankar and J. P. Gollub, Phys. Fluids A **2**, 1955 (1990).
[29] R. Ramshankar and J. P. Gollub, Phys. Fluids A **3**, 1344 (1991).
[30] P. Alstrøm, S. Andersen, W. I. Goldburg, and M. T. Levinsen (unpublished).
[31] W. Merzkirch, *Flow Visualization* (Academic, Orlando, 1987).
[32] This condition is derived for a ray originating along the axis of the optics. A ray near the edge will be limited to an asymmetric range of deflection angles about zero.
[33] Fluctuations are computed with respect to the average since we are interested in the disordered component.
[34] We achieve high wave number resolution by averaging the peak positions of many discrete Fourier transforms. Each transform is computed using a slightly different number of points from the same data set. This process shifts the bin positions slightly. The mean wave number is then extracted by averaging the peak wave numbers of the various transforms, each weighted by the fraction of power contained in the peak bin. The result is an estimate of the average wave number with higher resolution than the bin width of a single transform. This technique, which we have tested on artificial data, is superior to taking spectral moments when the width of the peak is comparable to the bin width.
[35] J. L. Lumley, in *Transition and Turbulence,* edited by R.

E. Meyer (Academic, New York, 1981), p. 215.
[36] M. V. Melander, H. S. Husain, and F. Hussain, in *New Perspectives in Turbulence* (Ref. [22]), p. 195.
[37] J. T. C. Liu, Annu. Rev. Fluid Mech. **21**, 285 (1989).
[38] N. Aubry, P. Holmes, J. L. Lumley, and E. Stone, J. Fluid Mech. **192**, 115 (1988).
[39] M. Dellnitz, M. Golubitsky, and M. Nicol, in *Trends and Perspectives in Applied Mathematics,* edited by L. Sirovich (Springer-Verlag, New York, 1994), p. 73.

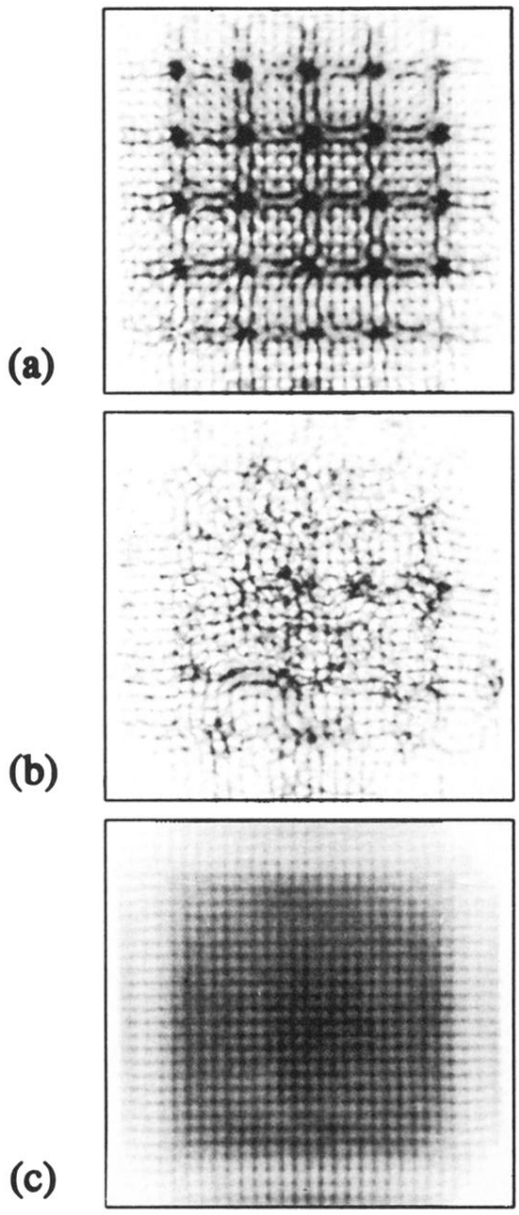

FIG. 1. Instantaneous and time-averaged images for square geometry (cell A, $f_0 = 55.75$ Hz). (a) Shadowgraph image of the time-independent wave pattern near onset ($\varepsilon = 0.05$). The wave pattern is approximately a mixed mode with mode numbers (29,6). (b) Instantaneous image of a chaotic pattern ($\varepsilon = 1.0$). (c) Time average over 12 800 images ($\varepsilon = 1.0$). The average reveals the probability distribution of antinode positions. High intensities are shown dark.

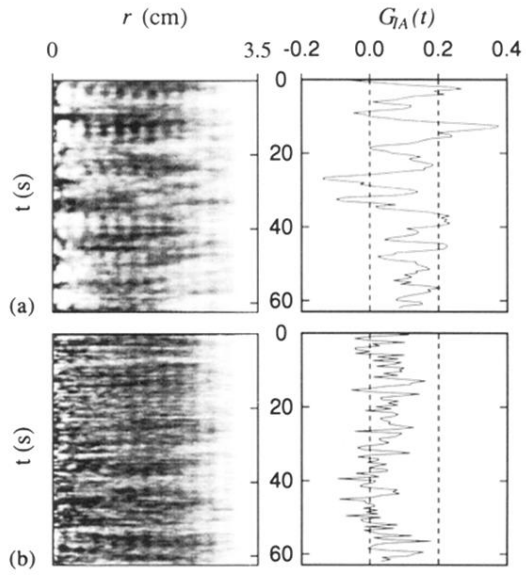

FIG. 12. Intensity-coded plot of the azimuthally averaged instantaneous images as a function of radius and time, and the corresponding cross correlation coefficient $G_{IA}(t)$ at (a) $\varepsilon=0.5$ and (b) $\varepsilon=1.0$. The data are from the circular cell C, $f_0=81$ Hz. When symmetric patches appear in the azimuthal average, they are phase coherent with the average.

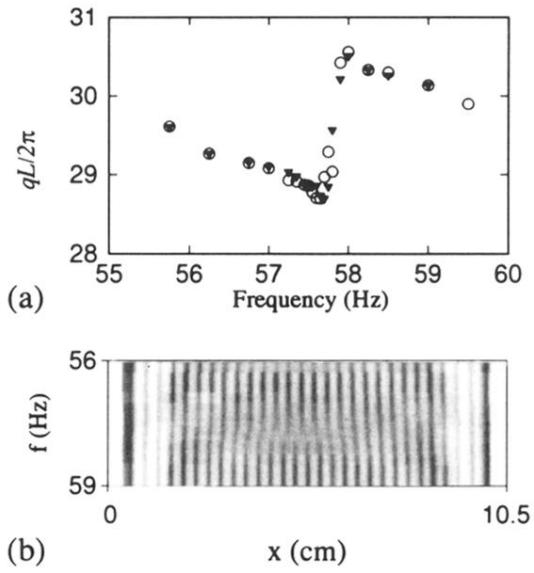

FIG. 16. (a) High resolution measurement of the mean wave number as a function of drive frequency near a wave number jump (square cell A, $\varepsilon = 1.0$) calculated over the central region of the cell, $L/4 < x,y < 3L/4$. The symbols correspond to increasing frequency (circles) and decreasing frequency (triangles). No hysteresis is observed. (b) Intensity coded plot of the y average of time-averaged images as a function of drive frequency, for the same data as in (a). The contrast decreases at the center of the cell for frequencies coincident with the observed jump in wave number.

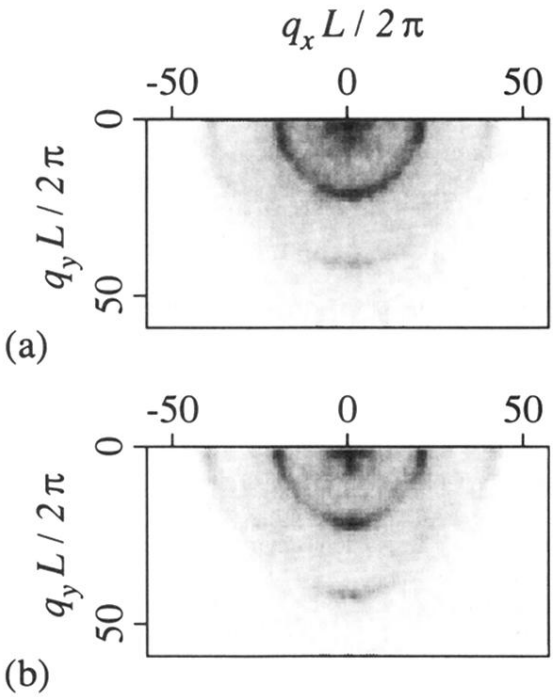

FIG. 17. Wave number spectra of instantaneous images at (a) $f_0 = 57.75$ Hz and (b) $f_0 = 58.5$ Hz in square cell A. The angular distribution is more uniform in case (a), coincident with the jump in the wave number (see Fig. 16).

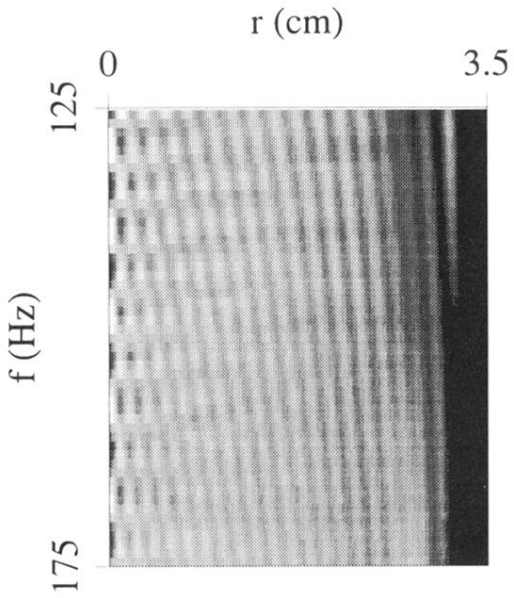

FIG. 20. Intensity coded plot of the average image in circular cell *C* as a function of radius and drive frequency (same data as Fig. 19). The average at the center of the cell can be a local maximum or a minimum, depending on frequency.

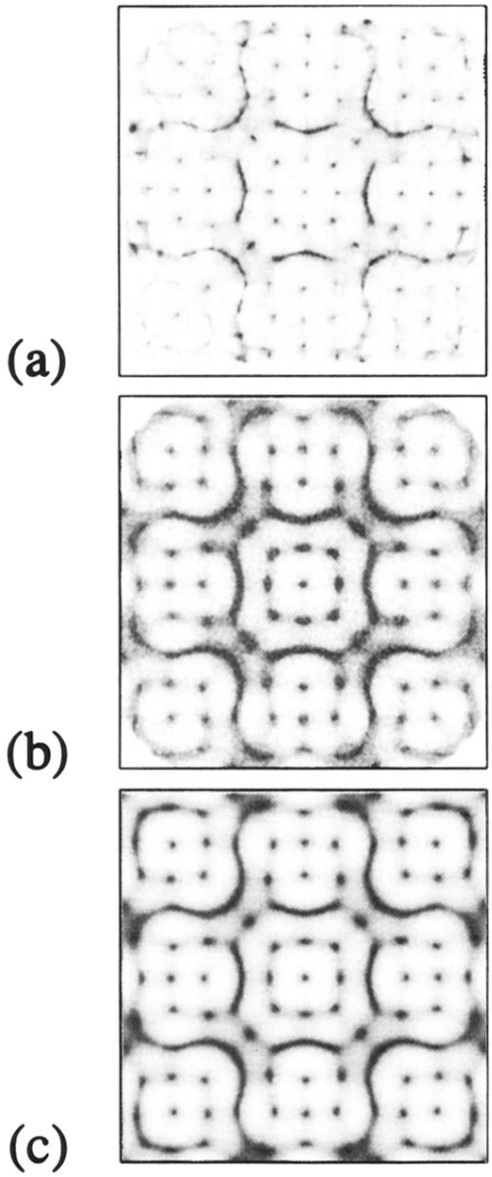

FIG. 3. Quantitative test of the imaging process. (a) Sample image of an onset pattern in the square cell. (b) Ray-tracing computation of the image, averaged over a cycle of the wave pattern. (c) Analytic approximation to the optical intensity $I_\delta(\vec{x})$ (Eq. 3.4). The waveform used is a positive mixed mode [Eq. (3.2)], with mode numbers (11,3). Bright spots in the image (shown dark here) appear at positions of small surface slope, i.e., at antinodes. The apparent wave number of the pattern is doubled.

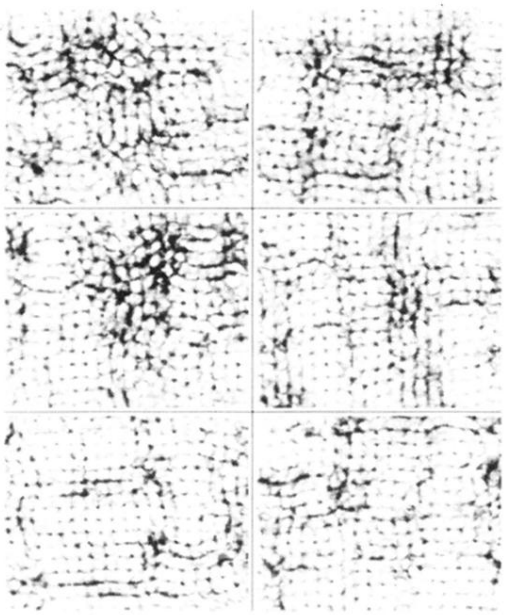

FIG. 4. Series of six instantaneous images of chaotic waves in square cell A at 4.5 s intervals ($f_0 = 55.75$ Hz, $\varepsilon = 1.0$). The central region of the cell is shown; time increases downward, then across.

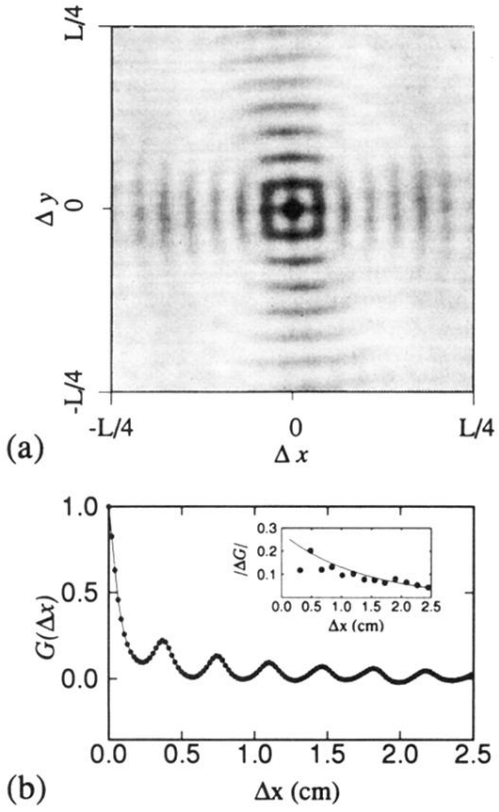

FIG. 5. Autocorrelation function, $G(\Delta\vec{x})$ of instantaneous images of chaotic waves (square cell A, $f_0=55.75$ Hz, $\varepsilon=1.0$). (a) Two-dimensional inverted gray scale image. (b) One-dimensional cut at $\Delta y=0$. The inset shows the peak-to-peak amplitude, and a fit to a decaying exponential. The correlation length is approximately 20% of the width of the cell.

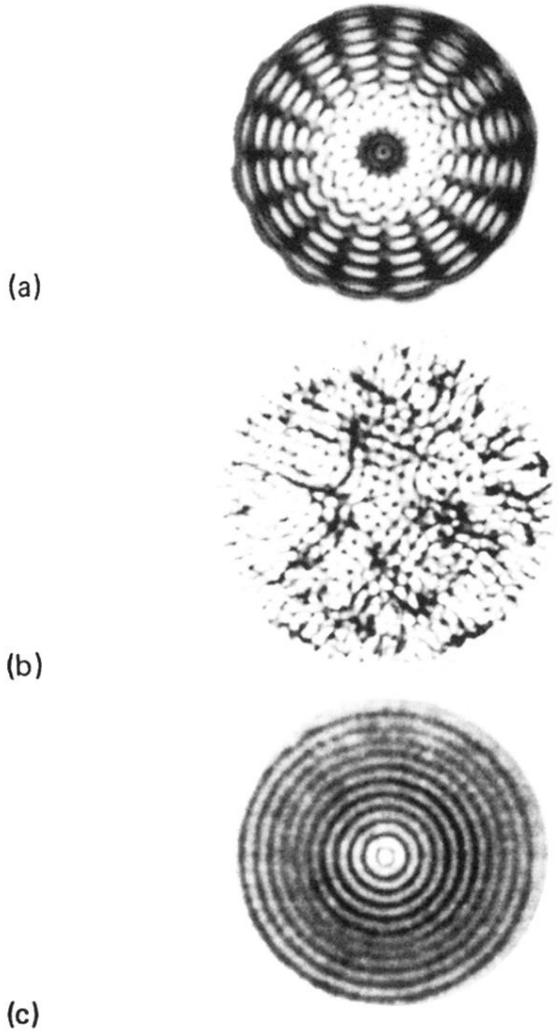

FIG. 7. Instantaneous and time average images for circular geometry (cell C, $f_0=81$ Hz). (a) Shadowgraph image of time-independent wave pattern near onset ($\varepsilon=0.01$). (b) Instantaneous image of a chaotic pattern ($\varepsilon=0.5$). (c) Time average over 12 800 images or ~ 15 min ($\varepsilon=0.5$).

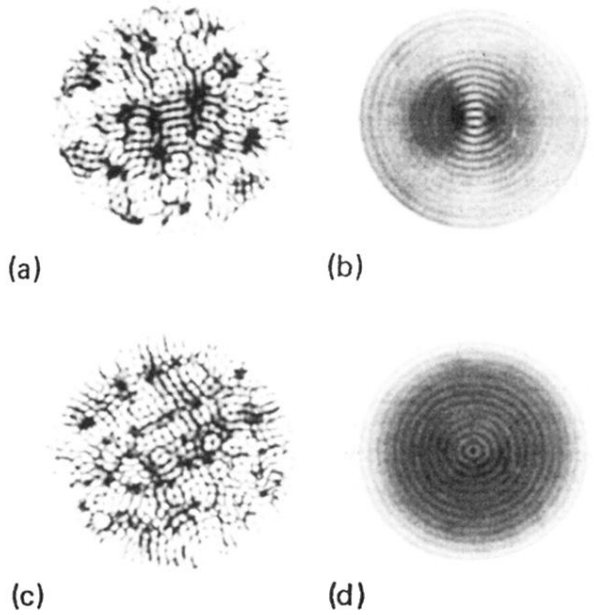

FIG. 8. Instantaneous [(a) and (c)] and time-averaged [(b) and (d)] images in a cell with elipticity 0.02 at $f_0 = 100$ Hz. [(a) and (b)] $\varepsilon = 0.15$; [(c) and (d)] $\varepsilon = 0.50$. The asymmetry of the resultant image is amplified at the lower drive amplitude, and is less pronounced at higher ε.

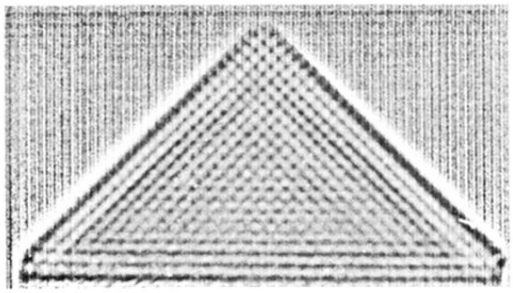

FIG. 9. Enhanced time-averaged image observed in the triangular cell E ($\varepsilon = 1.5$).